FINAL REPORT ON
AFOSR CONTRACT F49620-83-C-0064

Steven A. Orszag, Principal Investigator
Department of Mathematics
MIT
Cambridge, MA 02139

Volume 3

88 2 29 161

SECURITY CLASSIFICATION OF THIS PAGE

ADA191255

REPORT DOCUMENTATION PAGE

1a. REPORT SECURITY CLASSIFICATION	1b. RESTRICTIVE MARKINGS
Unclassified	

2a. SECURITY CLASSIFICATION AUTHORITY	3. DISTRIBUTION/AVAILABILITY OF REPORT
	Approved for public release; distribution is unlimited
2b. DECLASSIFICATION/DOWNGRADING SCHEDULE	

4. PERFORMING ORGANIZATION REPORT NUMBER(S)	5. MONITORING ORGANIZATION REPORT NUMBER(S)
	AFOSR-TR· 87-1390

6a. NAME OF PERFORMING ORGANIZATION	6b. OFFICE SYMBOL (If applicable)	7a. NAME OF MONITORING ORGANIZATION
MIT		AFOSR/NA

6c. ADDRESS (City, State and ZIP Code)	7b. ADDRESS (City, State and ZIP Code)
Department of Mathematics MIT Cambridge, MA 02139	Building 410, Bolling AFB DC 20332-6448.

8a. NAME OF FUNDING/SPONSORING ORGANIZATION	8b. OFFICE SYMBOL (If applicable)	9. PROCUREMENT INSTRUMENT IDENTIFICATION NUMBER
AFOSR/NA	NA	F49620-83-C-0064

8c. ADDRESS (City, State and ZIP Code)	10. SOURCE OF FUNDING NOS.			
Bolling Air Force Base Washington, DC 20332-6448	PROGRAM ELEMENT NO.	PROJECT NO.	TASK NO.	WORK UNIT NO.
Bld 410	61102 F	2307	A2	

| 11. TITLE (Include Security Classification) Final Report on AFOSR Contract F49620-83-C-0064 | | | | |

12. PERSONAL AUTHOR(S)
 - Steven A. Orszag

13a. TYPE OF REPORT	13b. TIME COVERED	14. DATE OF REPORT (Yr., Mo., Day)	15. PAGE COUNT
Final Report	FROM 2/1/83 TO 11/30/84	4 May, 1987	130

16. SUPPLEMENTARY NOTATION

17. COSATI CODES			18. SUBJECT TERMS (Continue on reverse if necessary and identify by block number)
FIELD	GROUP	SUB. GR.	Turbulence, Numerical Simulation

19. ABSTRACT (Continue on reverse if necessary and identify by block number)

We summarize work done under AFOSR Contract F49620-83-C-0064. The major results include: development of renormalization group techniques for large-eddy simulations of turbulent flows, the first direct numerical simulation of turbulent spots in channel and boundary-layer flows, the further development of spectral methods for turbulence simulations, the identification of secondary instability modes in free shear layers, the development of an efficient multi-grid marching method for solution of the parabolized Navier-Stokes equations, a mathematical analysis of boundary conditions for the parabolized compressible Navier-Stokes equations, the further development of a method to improve numerical solution of singular perturbation problems by use of asymptotic approximations.

20. DISTRIBUTION/AVAILABILITY OF ABSTRACT	21. ABSTRACT SECURITY CLASSIFICATION
UNCLASSIFIED/UNLIMITED ☑ SAME AS RPT ☒ DTIC USERS ☐	Unclassified

22a. NAME OF RESPONSIBLE INDIVIDUAL	22b. TELEPHONE NUMBER (Include Area Code)	22c. OFFICE SYMBOL
Dr James M McMichael	(202) 767-4936	AFOSR/NA

DD FORM 1473, 83 APR   EDITION OF 1 JAN 73 IS OBSOLETE.

NUMERICAL SIMULATION OF TURBULENT SPOTS
IN CHANNEL AND BOUNDARY LAYER FLOWS

By

Edward T. Bullister

Department of Mechanical Engineering,

Massachusetts Institute of Technology,

Cambridge, Mass. 02139

AND

Steven A. Orszag

Department of Applied and Computational Mathematics,

Princeton University, Princeton, New Jersey 08544

Abstract

The initiation and early growth of spots in channel and
boundary layer flows is simulated using a three dimensional
spectral code. The simulated spots show significant
agreement with available experimental data for such
quantities as growth rates and spreading angles.
Disturbances are introduced into the center and edge of the
developing channel spots to investigate the relative
sensitivity of spots.

1. INTRODUCTION

Emmons[1] was the first to observe turbulent spots in a laminar flow undergoing transition to a turbulent flow. Since then a large number of investigators have recognized the importance of spots in the study of both transition and turbulence. Naturally occurring spots are initiated by flow disturbances like noise. In the laboratory, spots may be artificially initiated with electric sparks or by injecting a jet of fluid. In a numerical simulation of spots, controlled disturbances may be imposed on a solution of the Navier-Stokes equations.

Soon after Emmons' discovery, Elder[2] noted that spots tend to grow independently of one another, even when they overlap. Gaster[3,4] studied the linear growth of small amplitude disturbances into a wave packet using both laboratory experiments and theoretical analysis. His theoretical predictions have been confirmed by laboratory observations so long as nonlinear effects are not important. Wygnanski, Sokolov, and Friedman[5] conducted an experimental study of spots in a boundary layer. Using conditional sampling techniques, they mapped out the geometry and growth rates of a spot as it develops in a boundary layer. Gad-el-Hak, et al.[6] conducted flow visualization experiments on boundary layer spots by injecting dye upstream of the spot initiation. They divided the spot into five regions(see Figure 1). Region I within the spot overhangs region II,

the laminar boundary layer below the head of the spot. Region III appears similar to a turbulent boundary layer. In regions IV and V the flow returns to a "calm" state. The photograph in Figure 2 illustrates the characteristic arrowhead shape of a boundary layer spot in streamwise-spanwise projection. This photograph was obtained by illuminating dye lines with a sheet of light very close to the wall.

The first detailed research directed toward investigating the characteristics of spots in a channel was conducted by Carlson, et al.[7] Using mica flakes to visualize the flow (Figure 3), they observed that a channel spot also has the characteristic arrowhead shape. They identified (see Figure 4) several features present in channel spots. The spreading half-angle (1) was about 8 degrees. The leading edges met at a sharp point and were preceded by oblique waves(7). The center of the spot (4) contained small scale turbulence. Streaks(3) trailed from region 4.

The purpose of the present study is to use direct numerical solution of the Navier-Stokes equation to identify details of the internal structure of spots, as well as to map out spot dimensions and growth rates. Comparison of our results for growth rates of the large-scale spot dimensions with those seen experimentally verifies that the essential growth mechanisms of spots is captured by our numerical experiments.

One previous study of numerical spots should be mentioned. Leonard[8] used discrete vortex methods to simulate numerically the early growth of a spot in a boundary layer. As with the present computations, the spots computed by Leonard are typically less mature than experimentally observed spots.

2. COMPUTATIONAL GEOMETRIES AND NUMERICAL METHODS

The computational domain that we use to simulate channel flow spots is as follows. In our simulations of channel flow spots, the flow is represented by 128x64x33 Fourier and Chebyshev modes in the x (streamwise), y (spanwise), and z (normal) directions, respectively (see Figure 5). The flow satisfies periodic boundary conditions in x and y and no-slip (rigid) boundary conditions at the walls ($z=\pm 1$). The computational box is nondimensionalized by the channel half-width; in the runs presented below, the physical box size is 20x5x2. With 128x64 resolution in x and y, the resultant node spacing (in physical space) of the spectral collocation points is $\Delta x=0.16$ and $\Delta y=0.08$.

For our boundary layer spot calculations, the flow is represented using 64 Fourier modes in x and y, with $\Delta x=2$ and $\Delta y=1$ (see Figure 6). In the z direction, the 33 collocation points are obtained by an algebraic mapping of the interval $[-1,1]$ to $[0,\infty]$ with half the collocation points located in the region $0<z<5$. The computational box is nondimensionalized by the boundary layer thickness $\eta=\sqrt{\nu x_0/U_\infty}$ at some representative x-location x_0. The periodic boundary conditions used in the streamwise direction are only approximate. They are justified because the increase in boundary layer thickness through the computational domain is only 6% (see also Balasubramanian, et al[9]). While inflow-outflow boundary conditions are, in principle, more realistic than periodic boundary conditions, they are more

wasteful of spatial resolution, which is the limiting factor in the present calculations.

The Navier-Stokes equations are solved in rotational form,

$$\frac{d\mathbf{v}}{dt} = \mathbf{v} \times \omega - \nabla(\Pi) + 1/\text{Re} \ \nabla^2(\mathbf{v})$$

$$\nabla \cdot (\mathbf{v}) = 0$$

where $\omega = \nabla \times \mathbf{v}$ is the vorticity and $\Pi = P + v^2/2$. The velocities are normalized with respect to the centerline velocity in the channel and the free stream velocity in the boundary layer.

The spectral method of Orszag and Patera[10] is used in both the channel and boundary layer calculations. For the boundary layer, the scheme is modified by mapping the Chebyshev collocation points of the channel to the desired locations in the boundary layer. A mapping function

$$z^* = f(z)$$

is chosen. When taking derivatives in the z-direction (e.g., in calculating the vorticity) the Chebyshev differentiation in z^* is followed by multiplication by $f'(z)$:

$$\frac{d}{dz} = \frac{df}{dz} \frac{d}{dz^*}$$

The boundary condition at infinity ($v_x - 1$) is implemented by recalculating the $(\cdot, 0)$ Fourier mode (the mean flow in x and y) in the viscous step. Symmetry is not imposed, but the spots develop symmetrically when symmetric initial conditions are used.

The disturbance is initiated by applying a body force to a packet of fluid, producing a small jet normal to and away from the wall. The form of the disturbance is Gaussian in x and y and continuous in time.

$$F = G(t) \, e^{[-r^2/2\sigma^2]}$$

where $G(t)$ is a ramp function. The size of the jets are indicated in Table I.

TABLE I

	Channel	B.L.
σ	0.16	0.7
Location	$0.1 < z < 0.2$	$0.05 < z < 1.5$
Peak normal Velocity	0.09	0.035

We impose the following boundary conditions on the flow through the channel: the velocity at the walls is zero, and the flow is periodic at the inflow/outflow and cross-stream

boundaries. The Reynolds number for the channel runs is
6000 based on the channel half-width. The Reynolds number
for the boundary layer simulations is 1000 based on the
boundary layer thickness corresponding to $\eta=1.0$.

3. SPOTS IN CHANNEL FLOWS

In Figure 7, we plot contours of the maximum (in y) of
the absolute value of the normal velocity, $\text{Max}_y |v_z|$ for a
channel spot at Re=6000. The contour plots we present for
channel spots encompass the entire 20x5x2 computational
domain; their dimensions are not to scale. Except where
noted, the contours are at 1% intervals of $\text{Max}_q |v_z|$, where q
is the coordinate normal to the plotting plane. With this
projection of the spot onto a plane we view the data from
the experimentalist's perspective (with the line of sight
extending all the way through the channel). At time t=1,
the initial disturbance has convected downstream and has
become slightly distorted. The initial peak velocity of
0.09 has decreased to 0.038 due to viscous diffusion. By a
time of t=3, the velocity has increased to 0.05 due to
instability in the flow. The disturbance is elongated in x
as well as convected downstream. In Figure 8 we see the
disturbance develop most of the features characteristic of a
spot. The front of the disturbance moves away from the
wall. The disturbance grows in all directions and the
"arrowhead" shape becomes apparent. The peak normal
velocity increases from 6% at t=12 to 9% at t=18.

In Figure 9 we show the development of the boundaries with an isometric view. Enclosed within the surface is fluid whose x velocity differs from the Poiseuille profile by more than 2%.

The results plotted in Figure 10 are $\text{Max}_y |v_z|$ and $\text{Max}_z |v_z|$. At t=30, the spot has fully extended through the channel with a peak normal velocity of 13%. The initial disturbance on the bottom wall has induced a new disturbance at the top wall. This second, smaller spot has a peak velocity that occurs at a distance of approximately 0.25 (1/8 channel width) away from the top wall. By t=30, the two spots have joined to produce a disturbance that fills the span of the channel.

In Figure 11 we show the distortion of the Poiseuille profile at the spot center. The velocity at the edge is essentially unchanged from that of the original Poiseuille flow, while at the spot center there is a velocity defect of 0.1-0.2. At the bottom wall, the shear has increased by a factor of 3.

In Table II and Figure 12, we show how the spot geometry changes in time. Although there are significant differences between conditions generating our numerical spot and those generating the spots studied experimentally, a comparison of numerical and laboratory features is instructive. Carlson et al[8] generated spots in a laboratory channel flow at Re=1000, while we used Re=6000 in our calculations. Most of the experimental data were taken more

than 50-100 channel widths downstream of the initial disturbance, while we have been able to follow the spot for only 10 channel widths. Further development of the channel spot would require a larger computational domain. The growth rate of the width and length of the numerical spot becomes constant at t=15 and remains so until the spot fills the domain at t=32. This steady growth rate is slightly higher than that observed experimentally in both the lateral and longitudinal directions. This discrepancy can be due to the difference in Reynolds numbers or to the lack of maturity of our computed spots compared to those studied experimentally. We have not observed in our data any significant evidence of the leading Tollmien-Schlicting waves that were observed experimentally. Again, we believe that the absence of these waves is due to the lack of maturity of our computed spots.

Table II Channel Spots

	Experimental		Computational
Velocity of Front	0.6		0.85
Rear	0.34		0.25
Spreading Half-Angle	8^{0}		10^{0}

A further numerical calculation was done to compare the stability characteristics of the spot at its edge and center. The velocity field of a spot at t=20 is used as the initial condition for three runs. The first run consists of the restarting the original spot calculation and allowing the spot to continue development undisturbed to a time of 24. For the second run, a disturbance is applied at t=20 to the original spot at its center. This disturbance is of the same spatial and temporal extent as the original disturbance that initiated the spot, but the magnitude is 1/10 that of the original. The difference between the resulting velocity fields, $\epsilon(x,t) = |\ v_{z1} - v_{z2}\ |$, is a measure of the effect of the disturbance. By t=24, $\epsilon(x,t)$ has exceeded 1% in the central 2/3 of the spot (Figure 13). The third run is identical to the second, but with the disturbance applied at the spot edge, rather than at the center. At t=24 the disturbance had propagated through most of the spot (see Figure 14), and had a peak magnitude of about 4%, as opposed to the 1.5% peak from the second run.

From these results, we conclude that channel spots are less stable at their edges than at their centers. This observation suggests that spots grow by destabilization of neighboring fluid, rather than simply engulfing laminar fluid.

4. SPOTS IN BOUNDARY LAYER FLOWS

In Figures 15 through 17 we show the development of a boundary layer spot at Re=1000 up to t=90. The contour plots we present for boundary layer spots encompass the entire 128x64 computational domain in x and y and are truncated at z=22. Again, except where noted, the contours are at 1% intervals of $Max_q |v_z|$, where q is the direction normal to the plotting plane. Figure 15 shows the streamwise and spanwise development of the spot from the initial disturbance. At t=90, the spot has begun to develop the characteristic arrowhead shape, which is more apparent in the second (2%) velocity contour. Figure 16 shows the development of the triangular shape and the overhang in the spanwise direction. Figure 17 shows the overhang develop in the leading edge.

Table III Boundary Layer Spots

	Experimental		Computational
Velocity of Front	0.9		0.85
Rear	0.5		0.3
Spreading Half-Angle	10°		12°

The growth and development of the spot in a boundary layer is compared with the experimental findings of Wygnanski, et al[5] in Table III. The growth rate of the spot

in the streamwise and spanwise directions is in relatively close agreement with the experimental data. This suggests that the growth mechanisms in a boundary layer spot have been accurately captured in this simulation.

Figure 18 shows cross sections of the spot at t=90. Here we plot contours of the local values of v_z at y-y_{center}=0.5, 2.5, and 4.5, in Figures 18a, 18b, and 18c, respectively. Intervals are at 1% and dashed contour lines represent negative z velocities. The velocities are highest in the plane closest to the center of the spot (see Figure 18a). Away from the spot centerline the velocities and the spot height decrease. The front of the spot has an overhang of a distance of 10-20 in x, as has been observed experimentally. The flow is dominated by eddies with length scales of approximately 10 in x and 5 in y. These length scales differ from those of unstable modes of the Orr-Sommerfeld equations, which predicts linear instability for much longer wavelengths, $30 < \lambda_x < 85$.

In order to explore the later time evolution of boundary layer spots, it will be necessary to use higher resolution simulations, which we hope to perform in the future.

CONCLUSIONS

It has been shown that spots can be generated by numerical solution of the Navier-Stokes equations. The fact

that our results for the growth rates of the large-scale spot dimensions are relatively close to those seen experimentally suggests that the essential growth mechanisms of spots have been captured by our numerical experiments. These simulated spots are less mature than typical experimental spots, but their behavior appears to approximate that in a fully developed spot.

The spots generated were not dominated by two dimensional Tollmien-Schlicting waves. This suggests that the growth in spots is not linear growth of two dimensional Tollmien-Schlicting waves. Moreover, the perturbation velocities seen were about 0.1; perturbations this large would make the results of linear theory inapplicable and suggest domination of nonlinear effects. This does not rule out the importance of Tollmien-Schlicting waves in the amplification of small disturbances which may develop into spots or as a driving mechanism for some secondary instability in spots.

ACKNOWLEDGEMENTS

References

[1]H. W. Emmons, J. Aero. Sci. **18**, 490(1951).

[2]J. Elder, J. Fluid Mech. **9**, 235(1960).

[3]M. Gaster and I. Grant, Proc. Royal Soc. **347**, 253(1975).

[4]M. Gaster, 1975 Proc. R. Soc. Lond. **347**, 271(1975).

[5]I. Wygnanski, M. Sokolov, and D. Friedman, J. Fluid Mech. **78**, 785(1976).

[6]M. Gad-el-Hak, R. Blackwelder, and J. Riley, J. Fluid Mech. **110**, 73(1981).

[7]A. Leonard, The Role of Coherent Structures in Modelling Turbulence and Mixing (ed. J. Jimenez). Lecture Notes in Physics, vol. 136, pp. 119-145. Springer(1981).

[8]D. R. Carlson, S. E. Widnall, and M. F. Peeters, J. Fluid Mech. **121**, 487(1982).

[9]R. Balasubramanian, S. Orszag, A. M. Cary, J. Lin, M. Walsh Submitted to the J. Fluid Mech.

[10]S. Orszag and A. T. Patera, J. Fluid Mech. **128**, 347(1983).

FIG. 1 Schematic of an experimental boundary layer spot cut through the center (from Gad-el-Hak et al.[6]).

FIG. 2 Visualization of an experimental boundary layer spot using fluorescent dye and a sheet of laser light at the wall; $Re_x = 5 \times 10^5$ (from Gad-el-Hak et al.[6]).

FIG. 3 Visualization of an experimental channel spot using mica platelets (from Carlson et al.[8]).

FIG. 4 Channel spot schematic: (1) spreading half angle; (2) trailing streaks; (3) region of small-scale turbulence (4) oblique Tollmien-Schlicting waves (from Carlson et al.[8]).

FIG. 5 Channel geometry and nomenclature. Channel is 20x5x2 in the x,y, and z directions, with 128x64 Fourier modes in x and y and 33 Chebyshev modes in z.

FIG. 6 Boundary layer geometry and nomenclature. Boundary layer computational domain is 128x64 in the x and y directions, with 64x64 Fourier modes in x and y and 33 Chebyshev modes mapped in the normal(z) direction.

FIG. 7 Early-time evolution of channel spot. $Max_y |v_z|$ contours are plotted at 1% intervals.

FIG. 8 Channel spot at intermediate times. $Max_z |v_z|$ contours in a) and b); $Max_y |v_z|$ contours in c) and d).

FIG. 9 Surfaces of 2% x-velocity perturbations in developing channel spot.

FIG. 10 Channel spot at t=30. $Max_z |v_z|$ contours in a); $Max_y |v_z|$ contours in b).

FIG. 11 Mean velocity profiles at center (solid) and edge (broken) of spot.

FIG. 12 Location in x of front, center, and rear of channel spot vs. time, where spot is defined as region where $|v_z| \geq 2\%$. For t larger than 30, the spot length reaches the periodicity length of the computational domain, so the spot ceases to grow in the streamwise direction.

FIG. 13 Perturbation velocity, $\epsilon(x,t)$, contours at t=22 and t=24 for channel spot perturbed at its center at t=20.

FIG. 14 Perturbation velocity, $\epsilon(x,t)$, contours at t=22 and t=24 for channel spot perturbed at its edge at t=20.

FIG. 15 Development of boundary layer spot. $\text{Max}_z |v_z|$ contours are plotted at 1% intervals. a)t=30; b)t=60; c)t=90

FIG. 16 Development of boundary layer spot. $\text{Max}_y |v_z|$ contours are plotted at 1% intervals. a)t=30; b)t=60; c)t=90

FIG. 17 Development of boundary layer spot. $\text{Max}_x |v_z|$ contours are plotted at 1% intervals. a)t=30; b)t=60; c)t=90

FIG. 18 Slices of spot at t=90. Contours of v_z at y=32, 30, and 28. The plane of symmetry of the spot is at y=32.5. Dotted lines represent negative v_z.

Figure 1

Flow

Figure 2

Figure 3

Flow direction
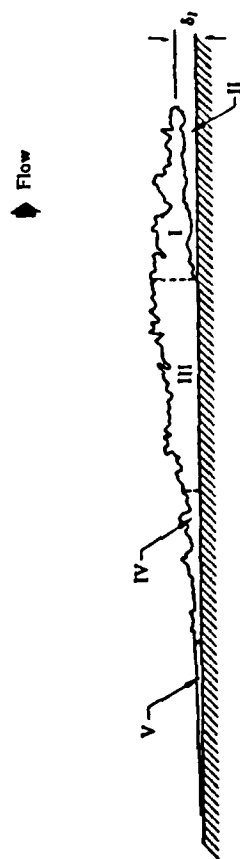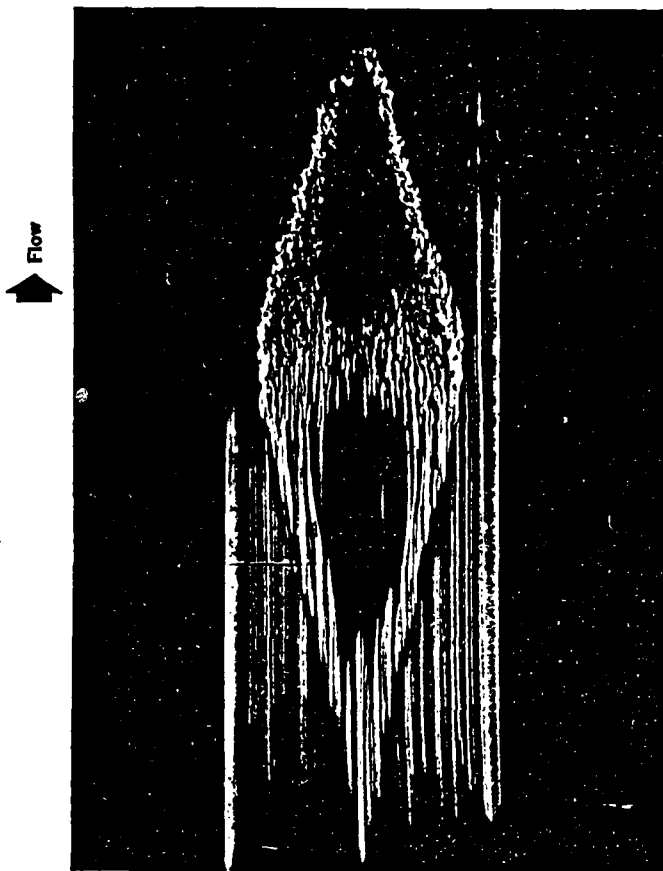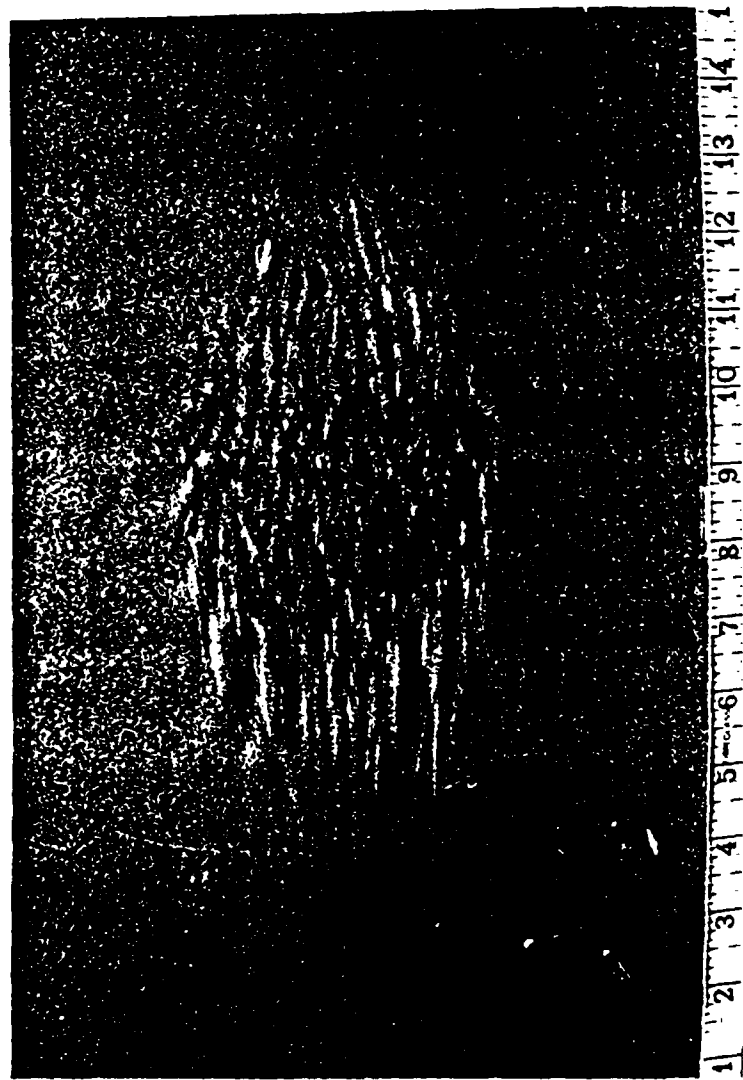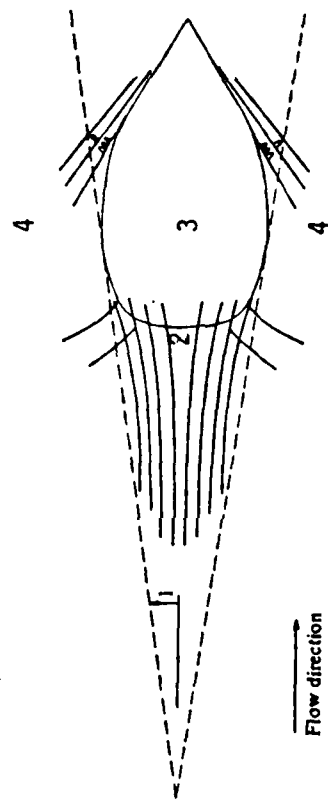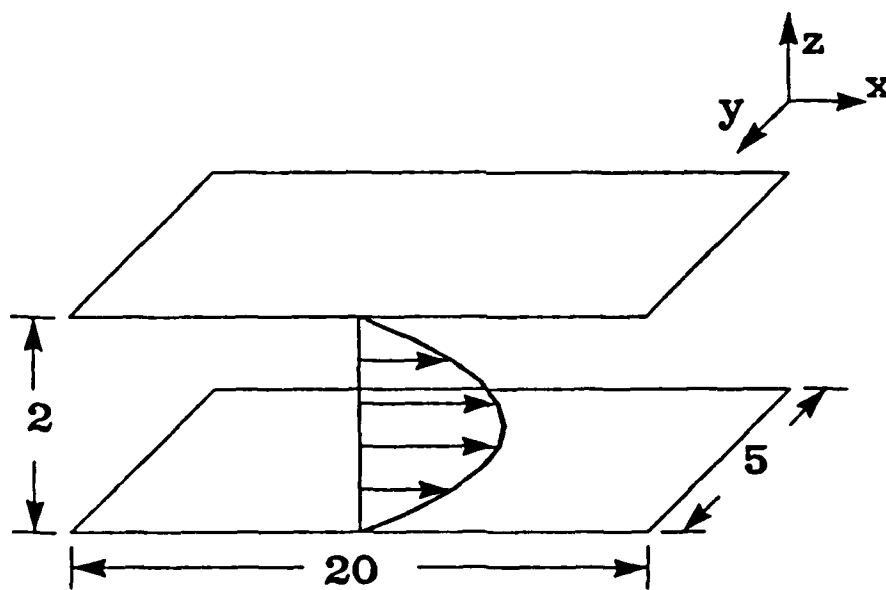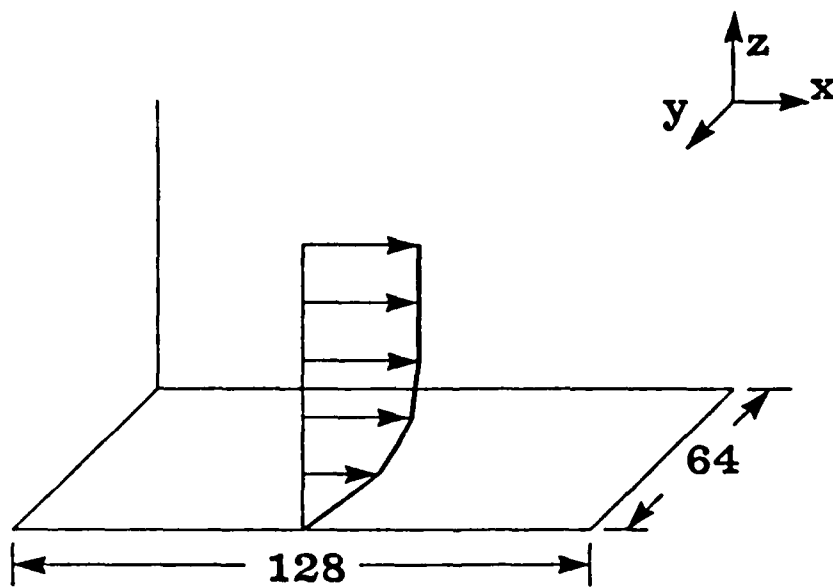
Figure 4

Figure 5

Figure 6

Early-Time Spot Evolution at R = 6000

TIME

1
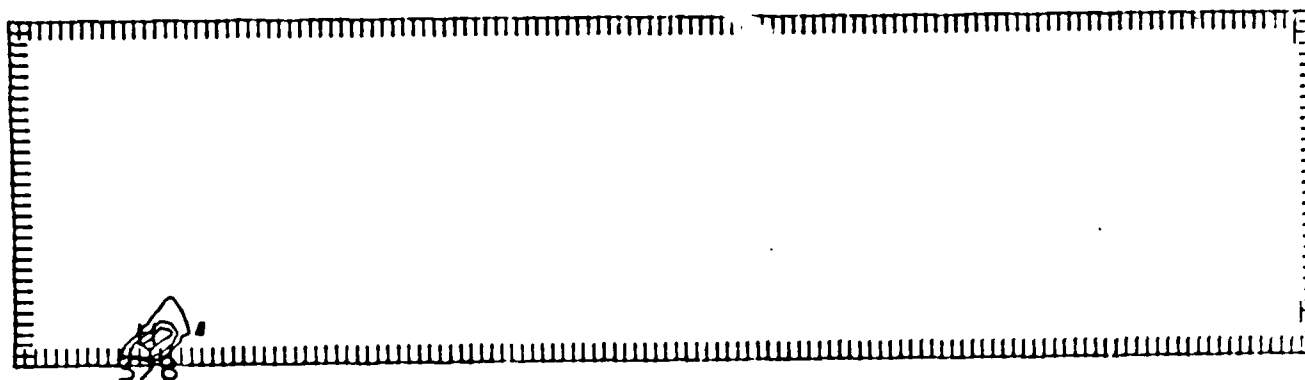
3
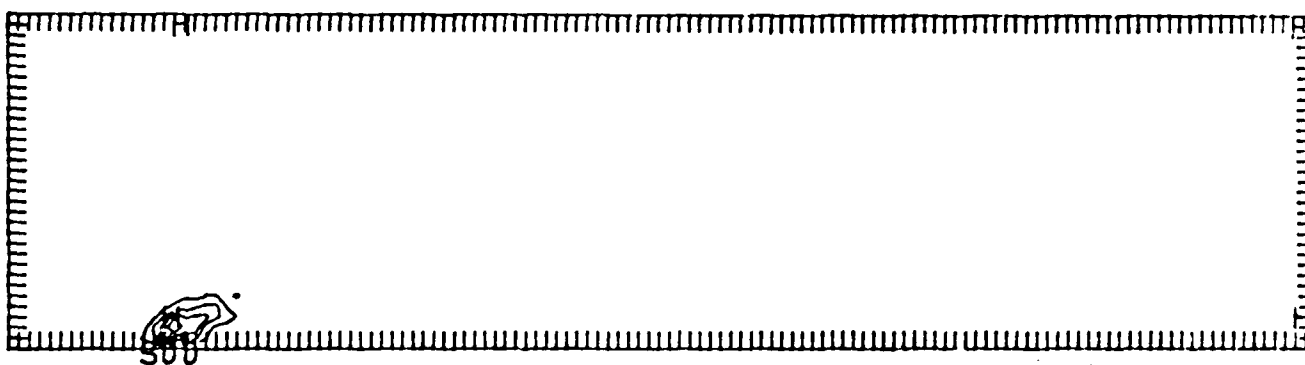
6
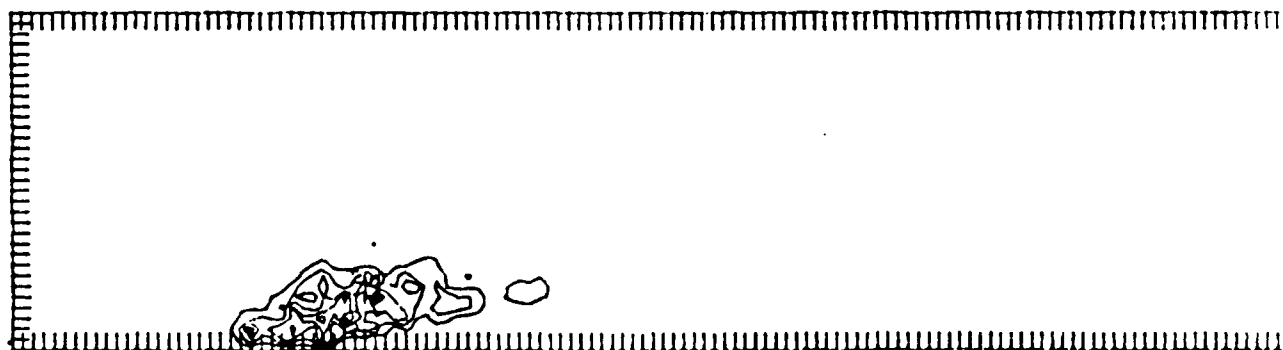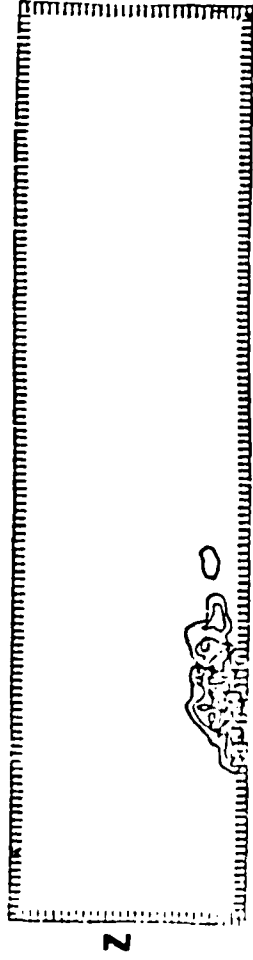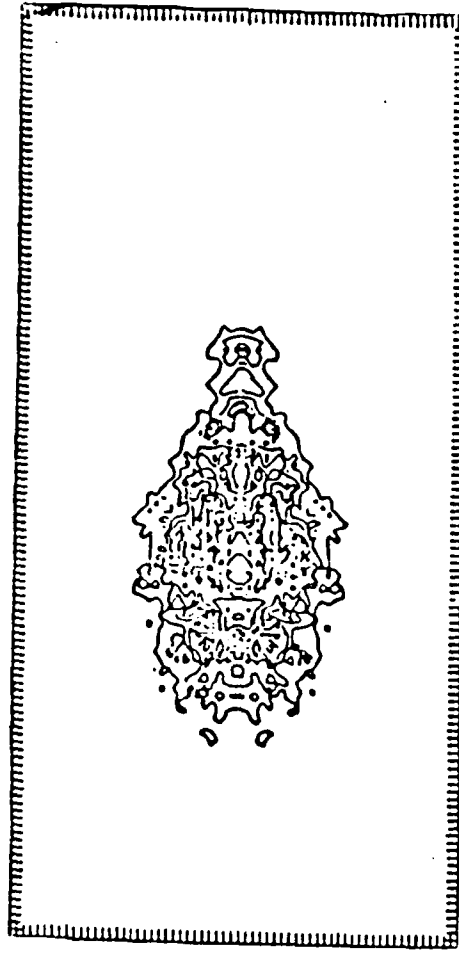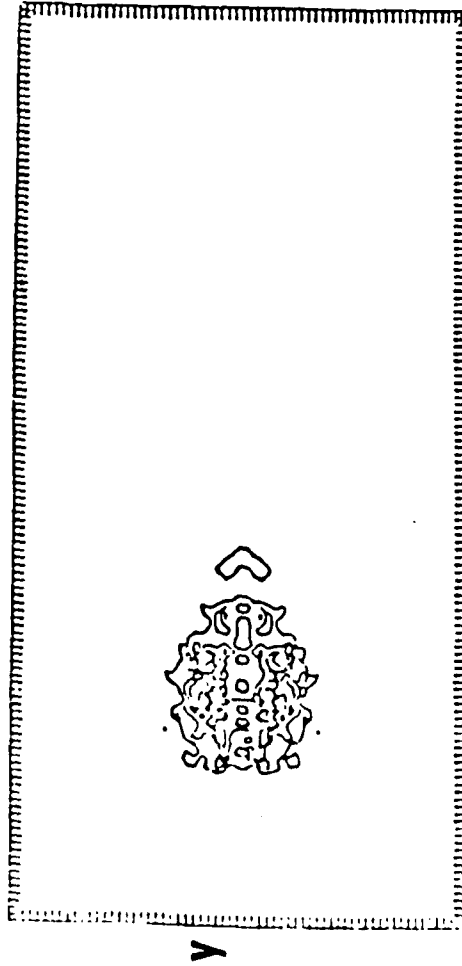
CONTOUR FROM 0.00000   TO 0.60000E-01

Figure 7

t=18

t=12

z

y

x

x
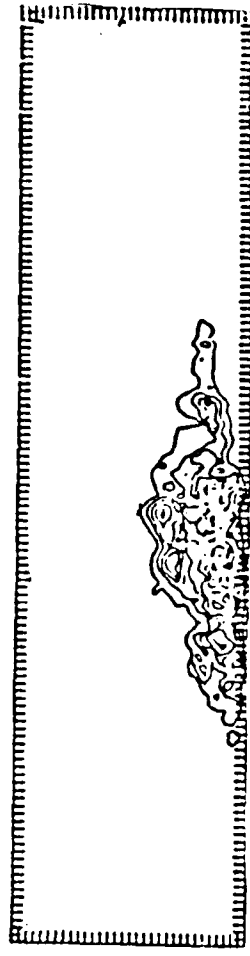
Figure 8

Surfaces of 2% x-Velocity Perturbation
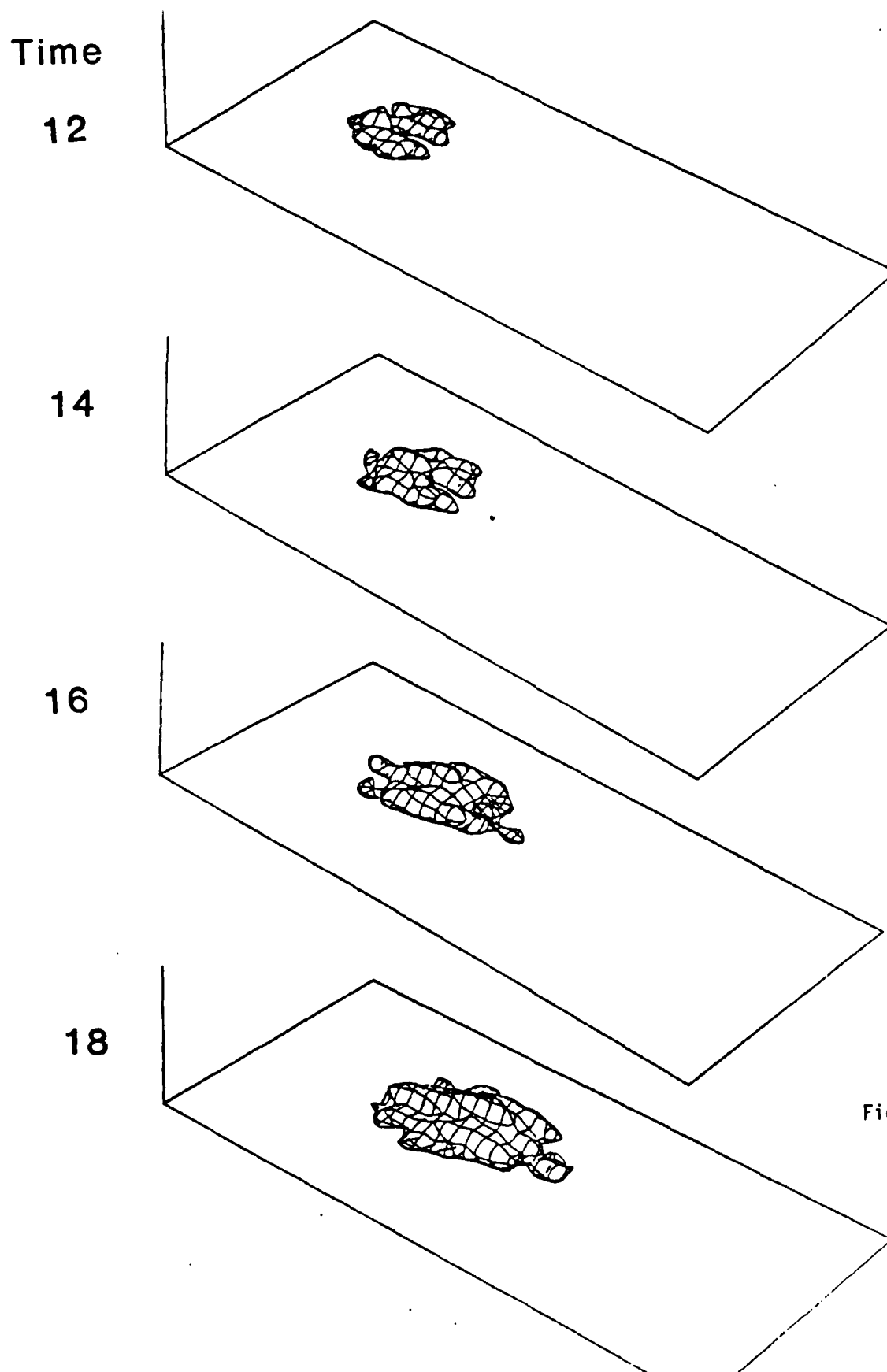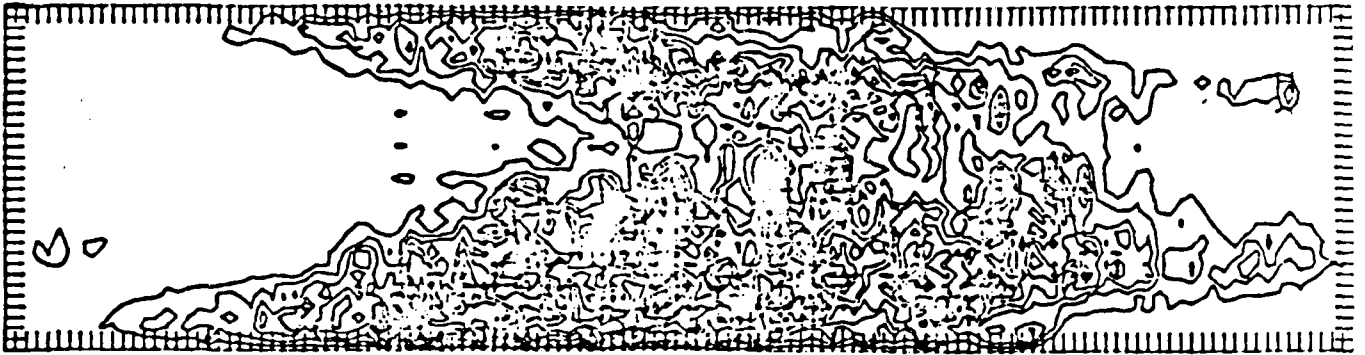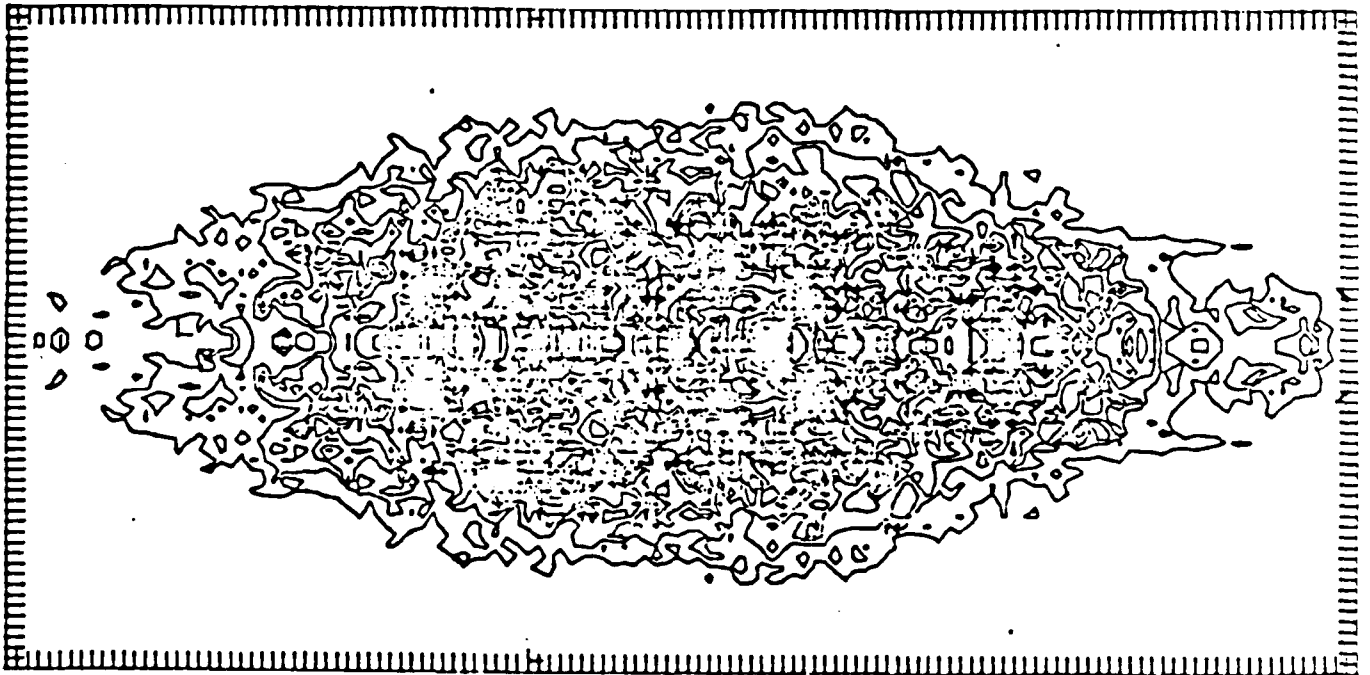
Time

12

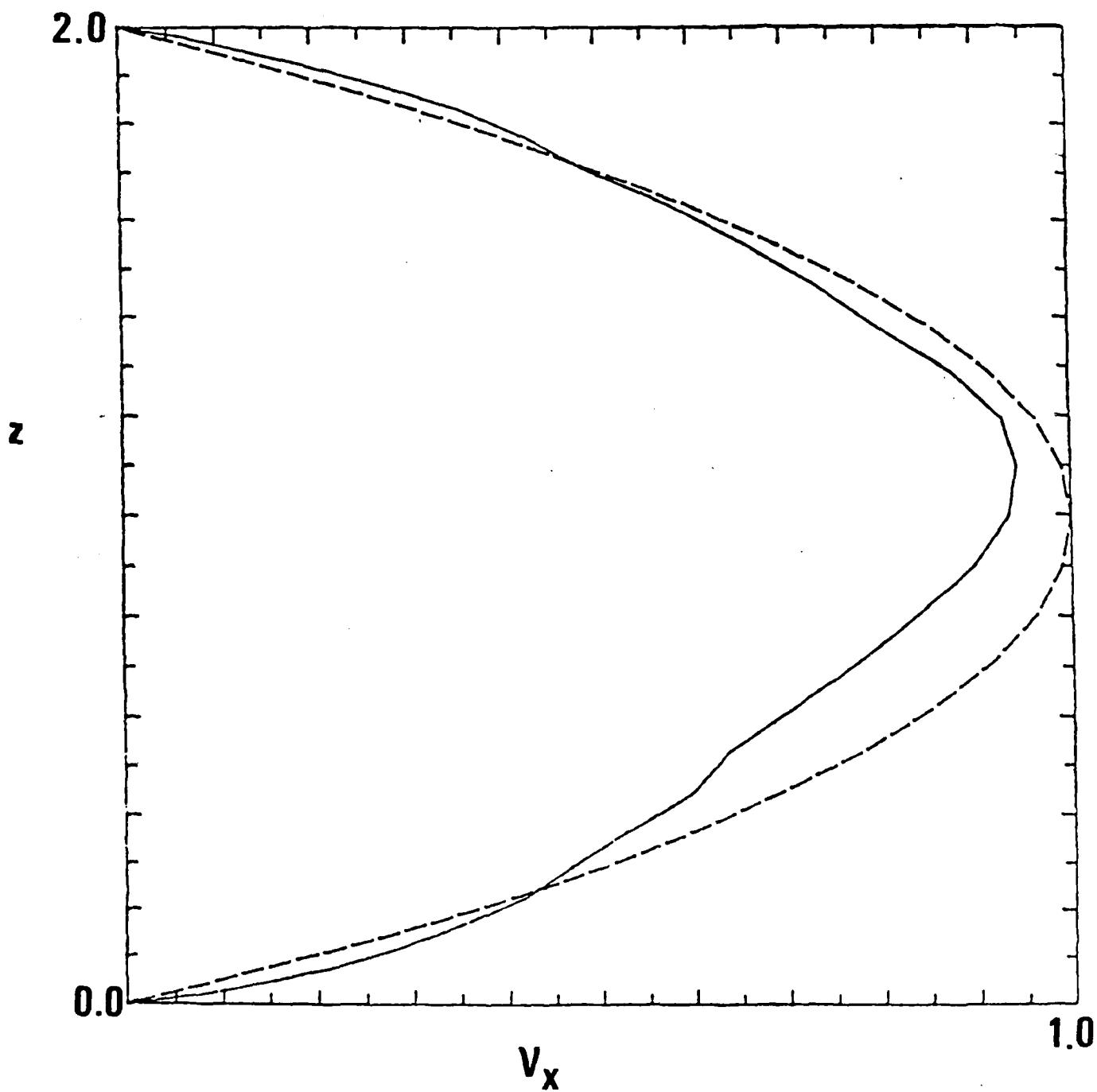14

16

18

Figure 9

t = 3 0

z

y

X

Figure 10

MEAN VELOCITY PROFILES

AT CENTER AND EDGE OF SPOT

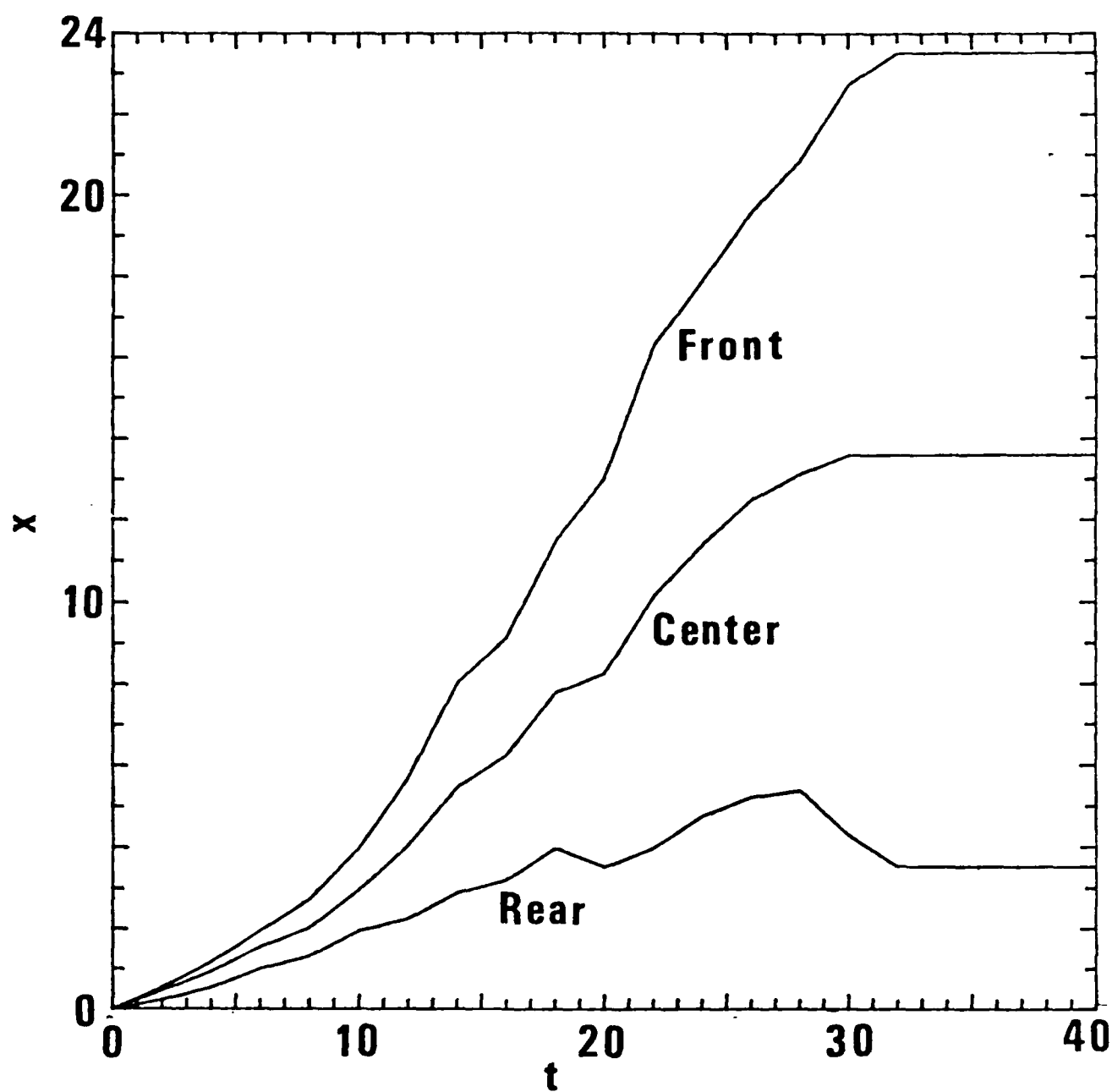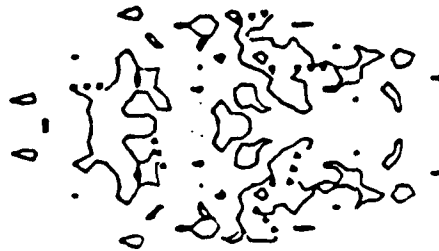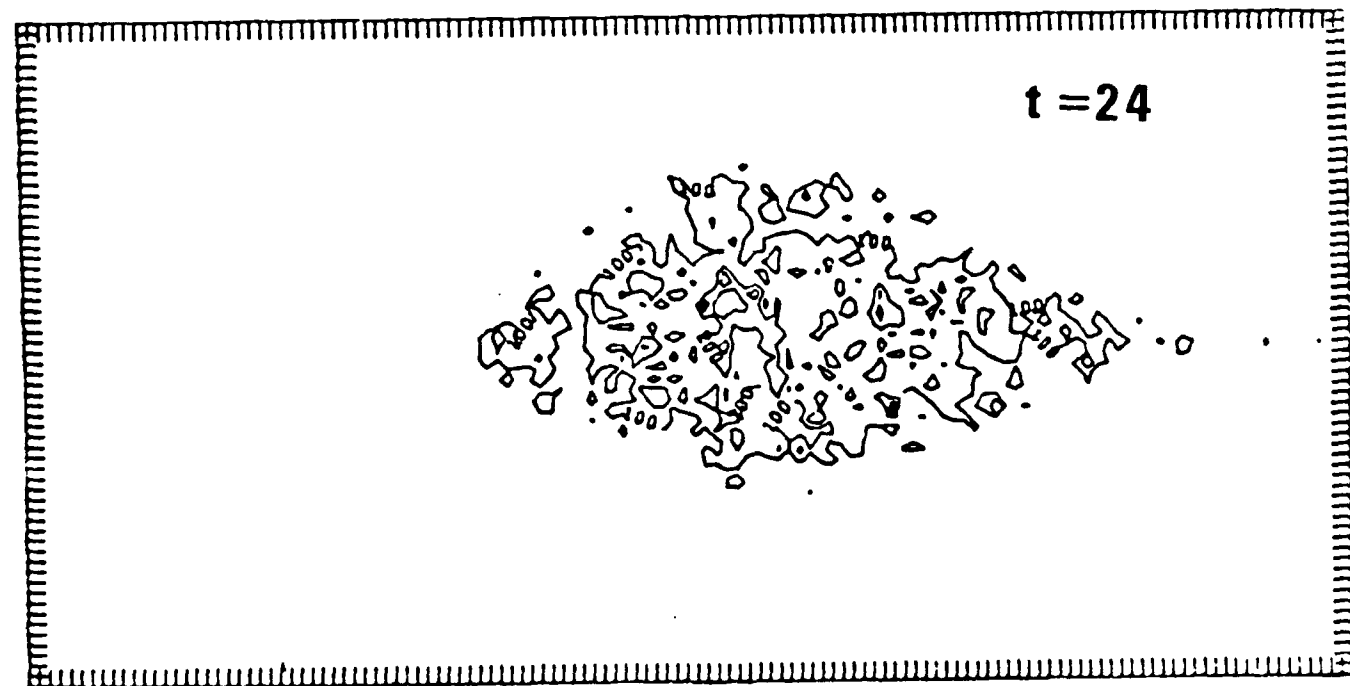Figure 11

Figure 12

t=22

t=24

X

Figure 13

t=22

t =24

y

x

Figure 14

t = 30

y

X

Figure 15a

t = 60

y

x
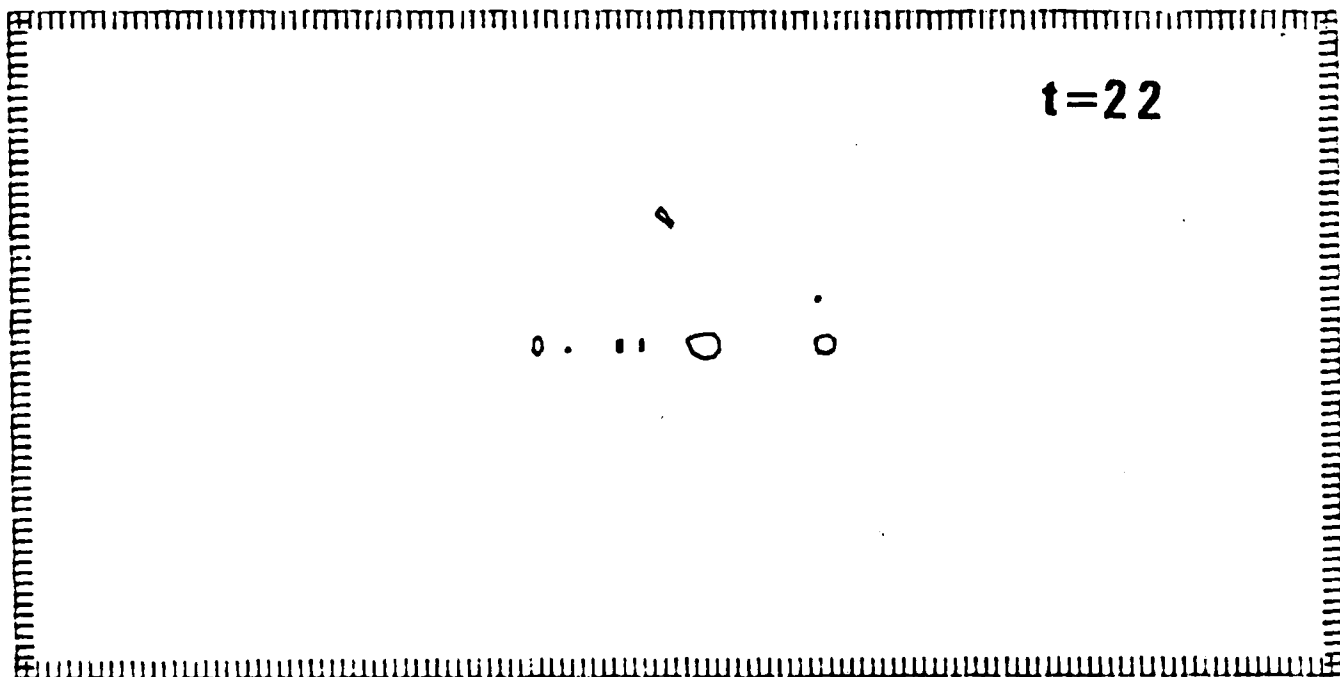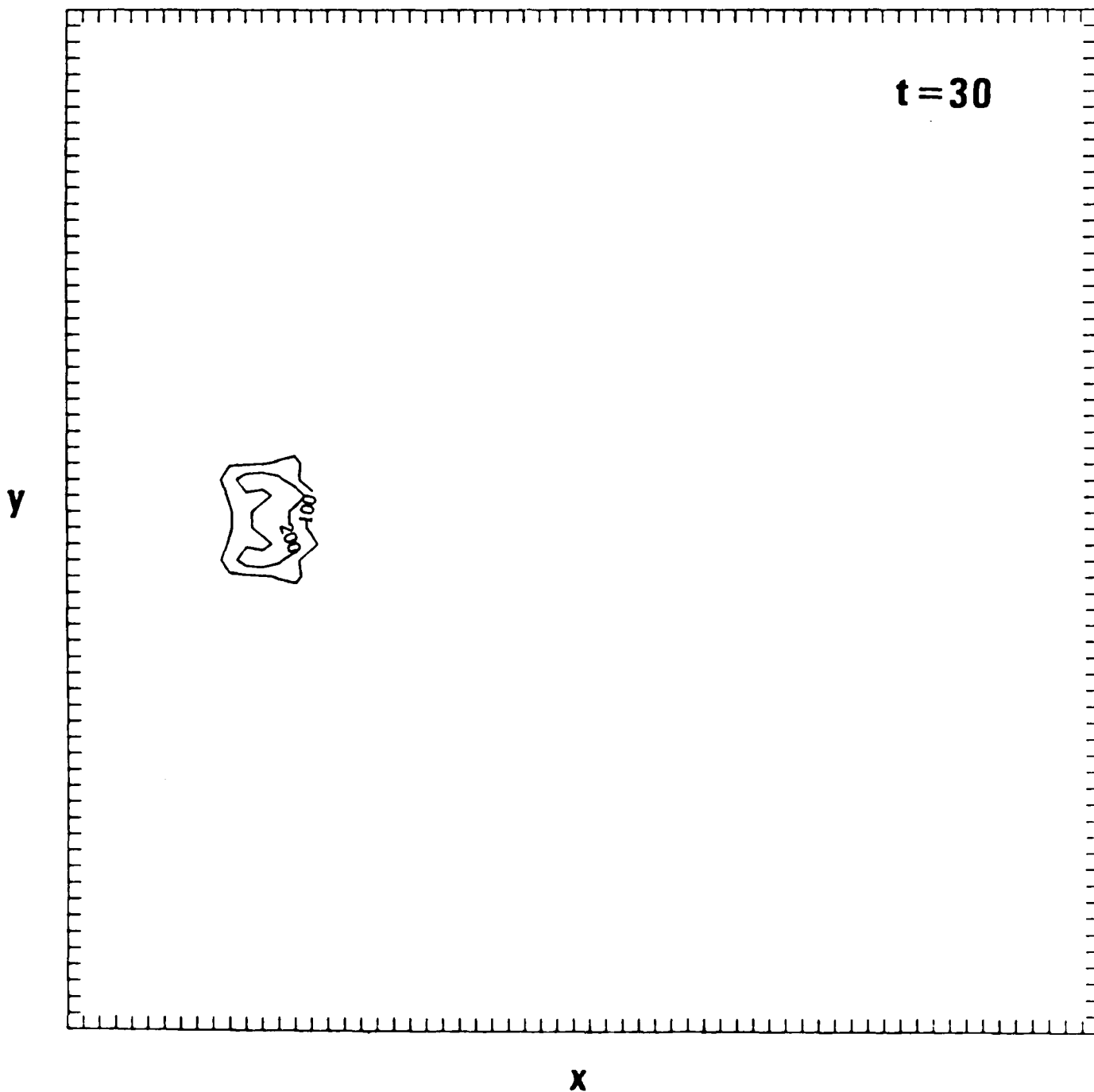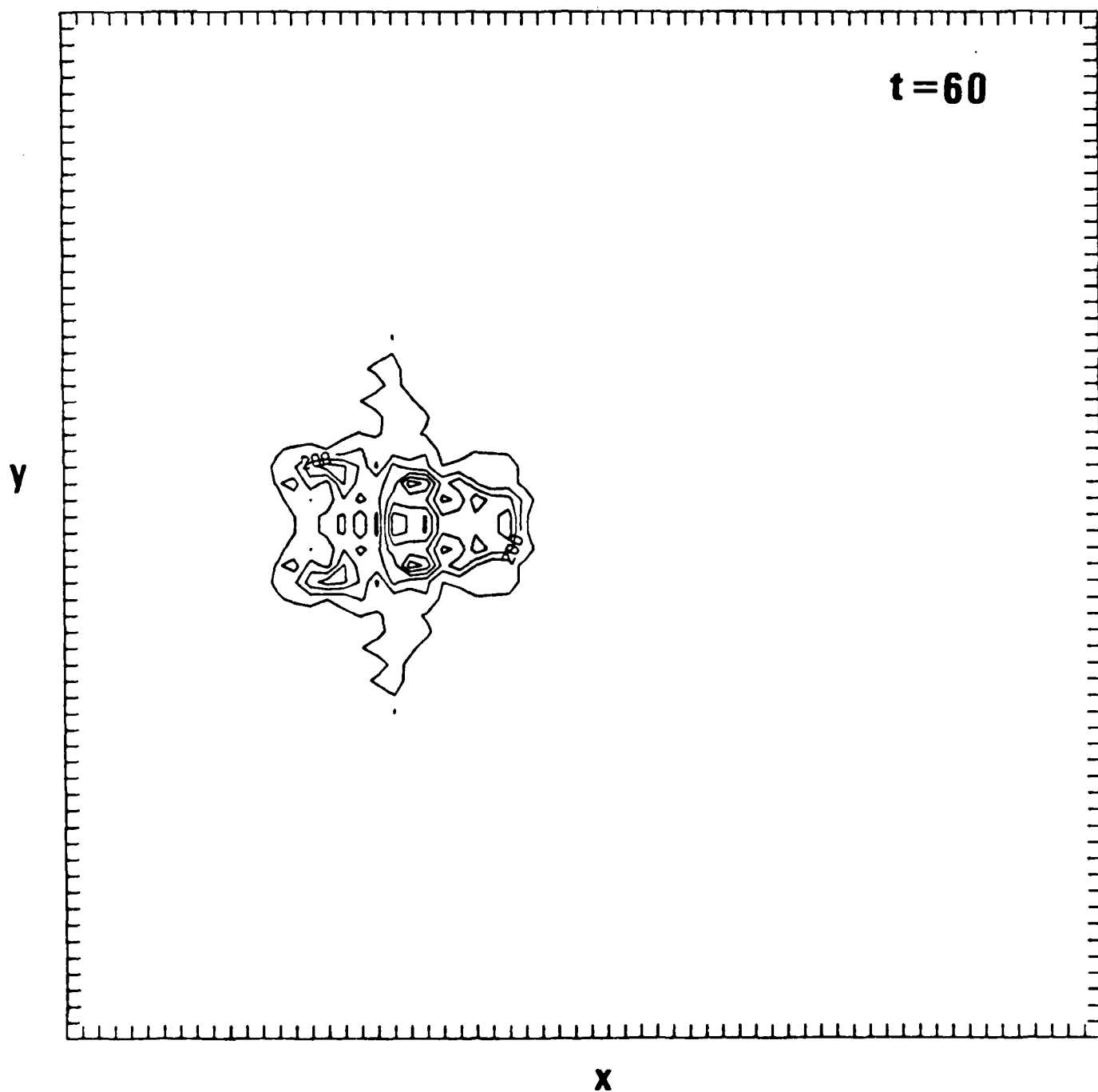
Figure 15b

Figure 15c

Figure 16

t = 30

(a)

t = 60

(b)

t = 90

y

(c)
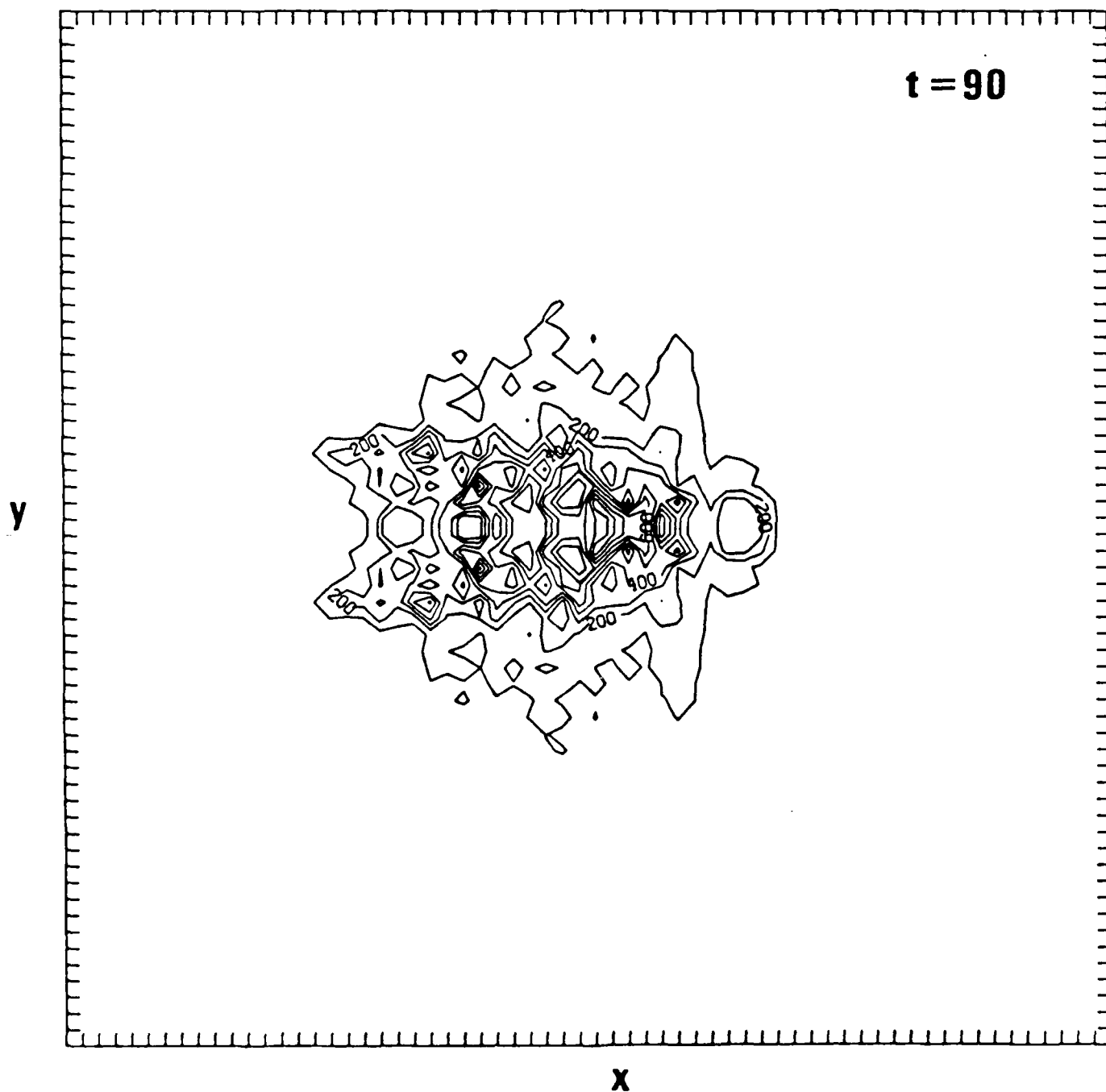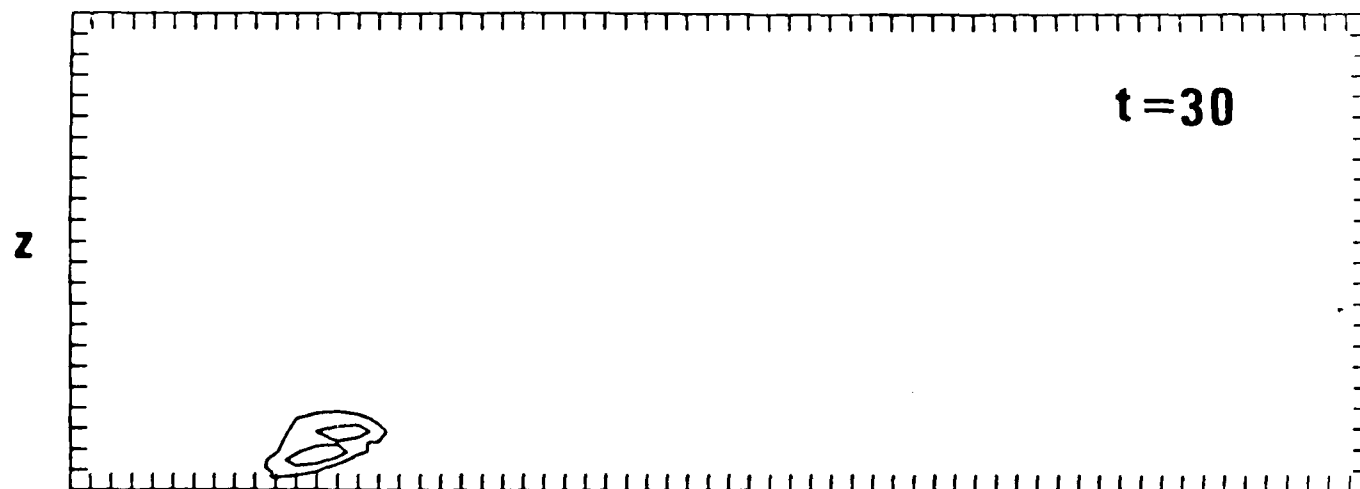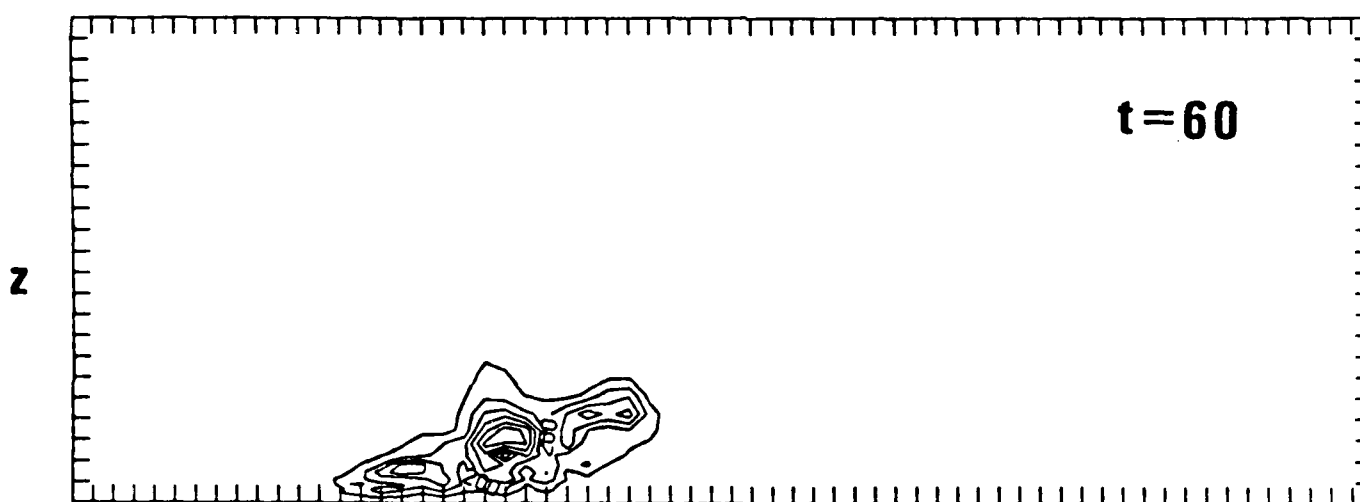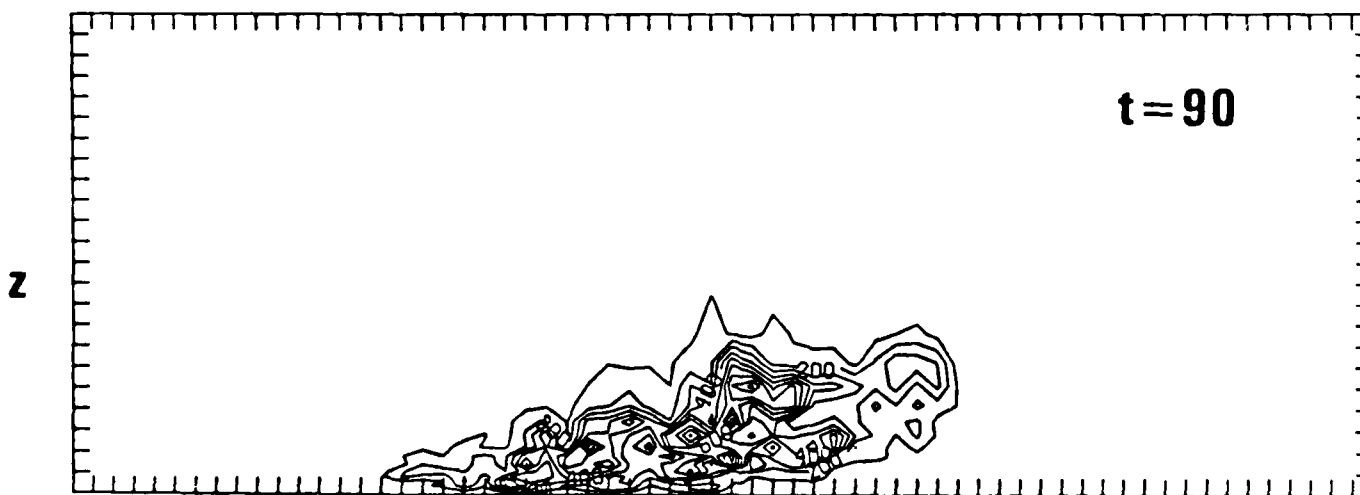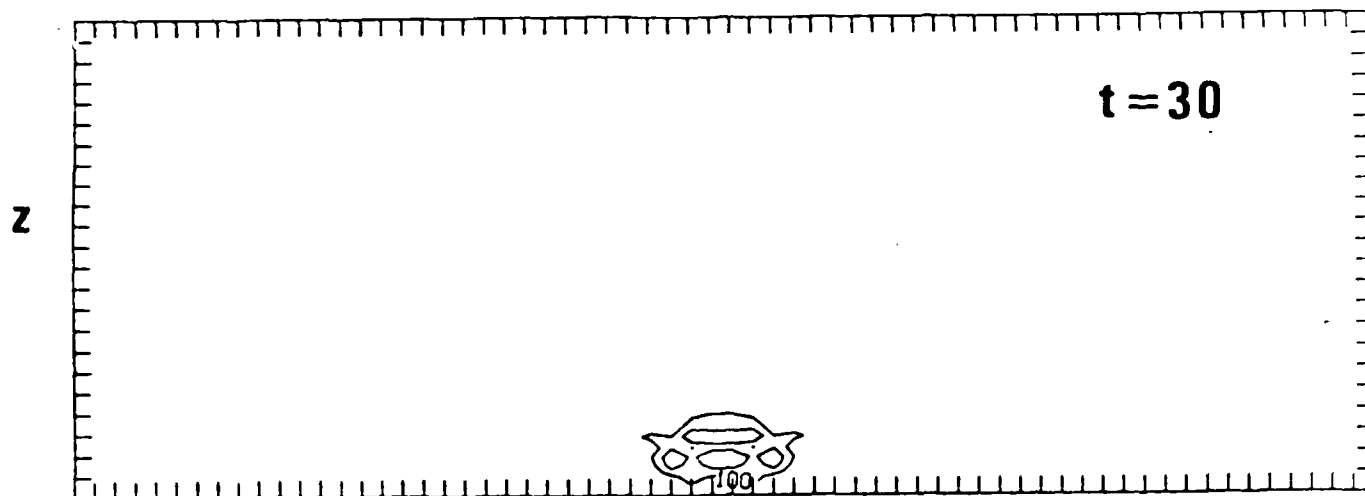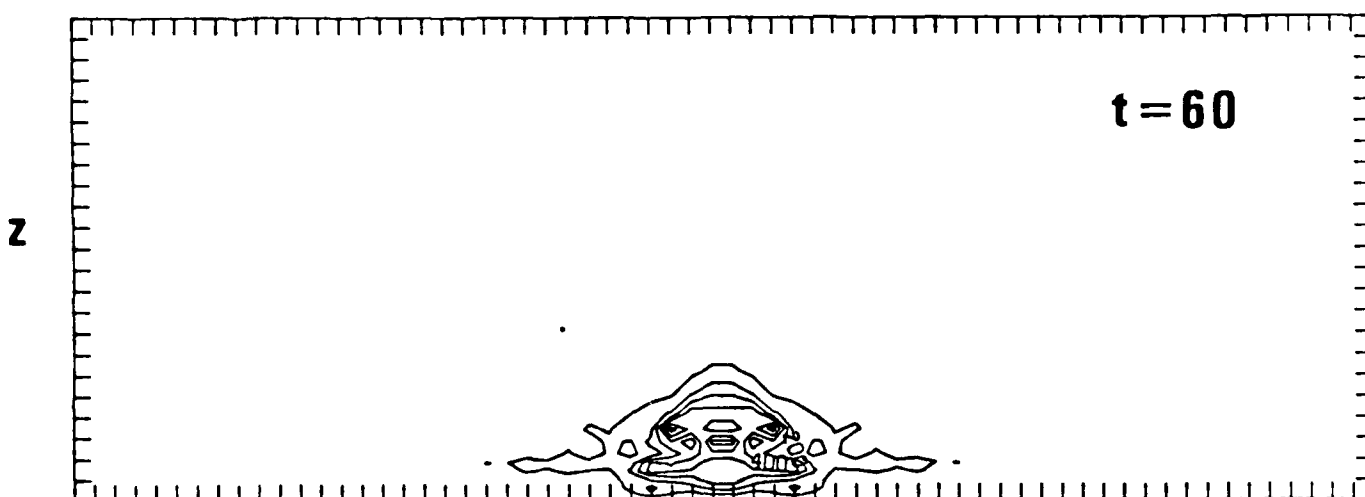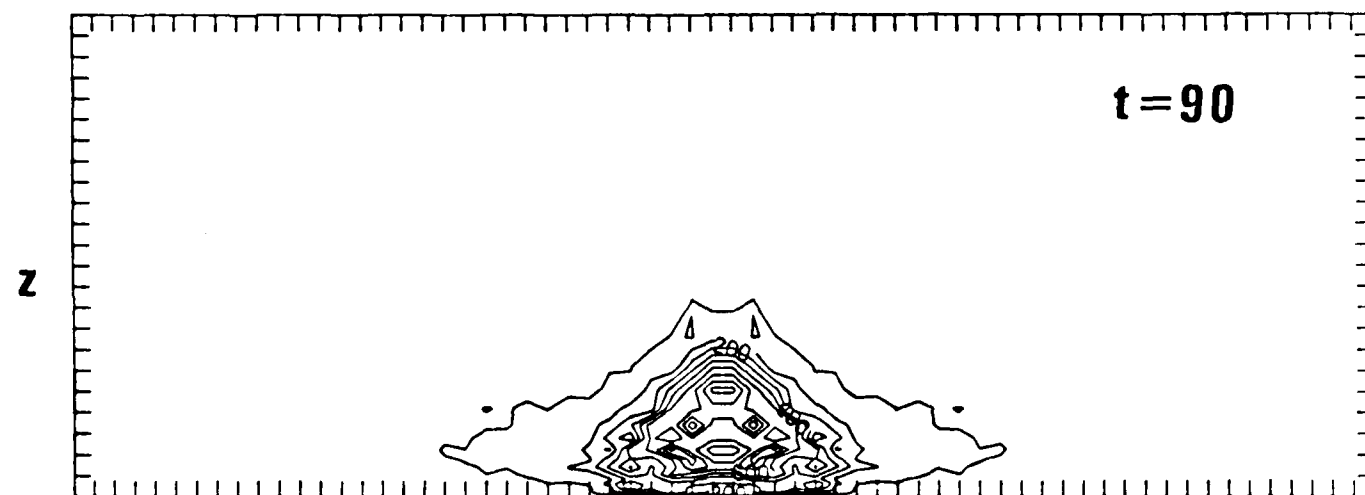
Figure 17

t=90

z

y=32

(a)

z

y=30

(b)

z

y=28

X

(c)

Figure 18

Numerical Solution of Incompressible Flows by a Marching Multigrid Nonlinear Method

Moshe Rosenfeld* and Moshe Israelit†

Technion-Israel Institute of Technology, Haifa, Israel

A downstream marching iterative scheme for the solution of the steady, incompressible, and two-dimensional parabolized or thin layer Navier-Stokes equations is described for a general curvilinear orthogonal coordinate system. Modifications of the primitive equation global relaxation sweep procedure result in an efficient marching scheme. This scheme takes full account of the reduced order of the approximate equations as it behaves like the SLOR method for a single elliptic equation. The proposed algorithm is essentially Reynolds number-independent and therefore can be applied to the solution of the incompressible Euler equations. A judicious choice of a staggered mesh enables second-order accuracy even in the marching direction. The improved smoothing properties permit the introduction of multigrid acceleration. The convergence rates are similar to those obtained by the multigrid solution of a single elliptic equation; the storage is also comparable as only the pressure has to be stored on all levels. Numerical results are presented for several boundary-layer-type flow problems, including the flow over a spheroid at zero incidence.

I. Introduction

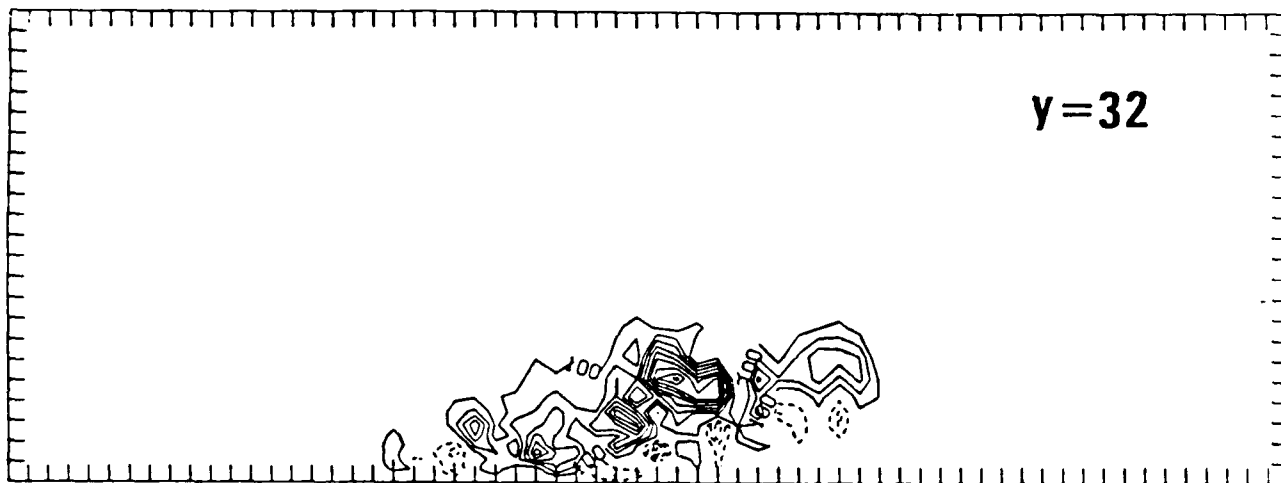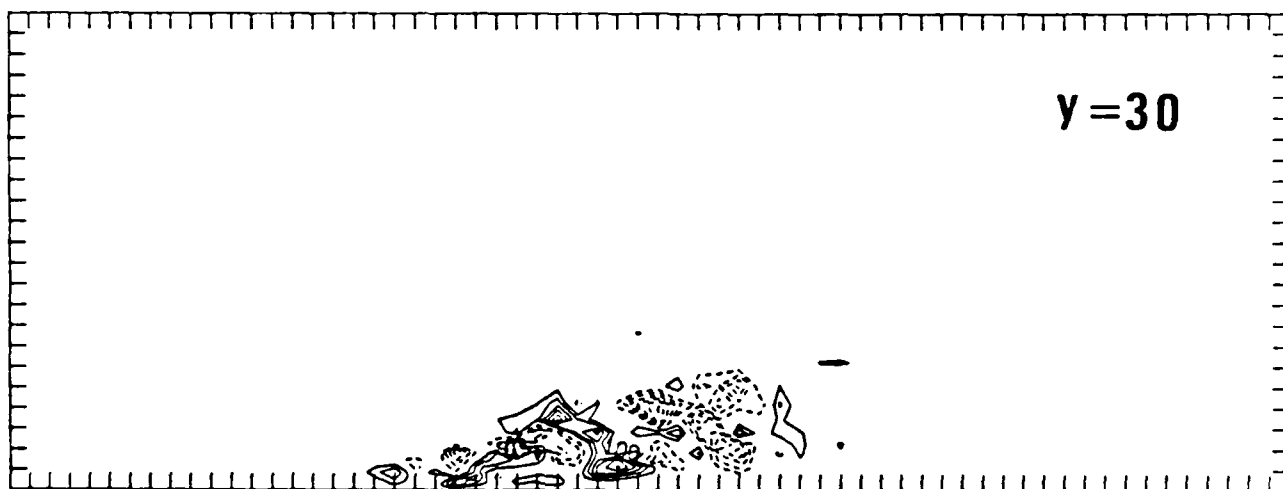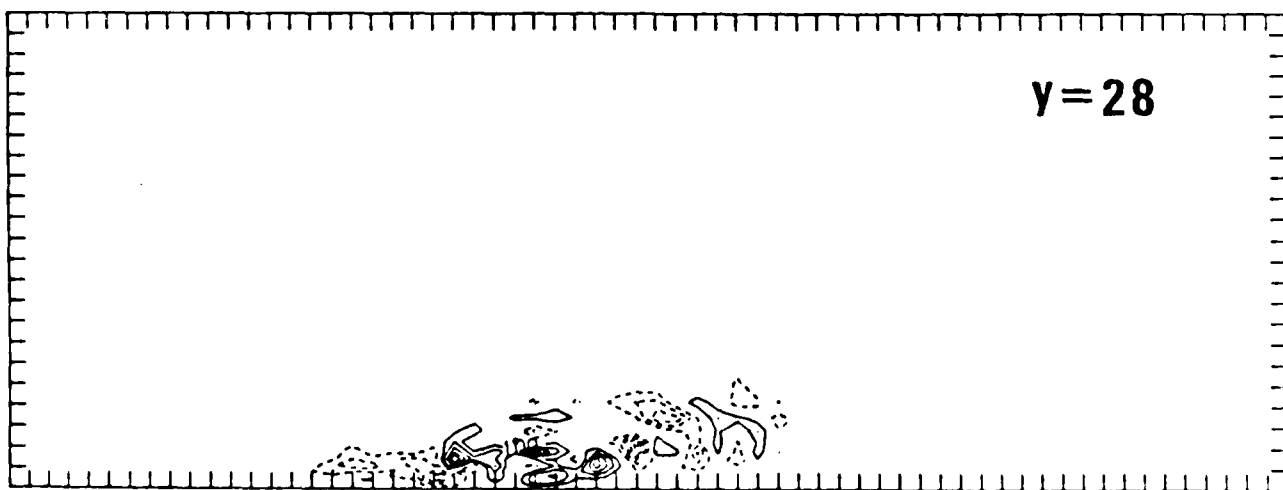CONSIDERABLE evidence has accumulated recently about the applicability of the parabolized Navier-Stokes (PNS) equations for high Reynolds number flows with a principal flow direction (see Rubin[1]). The PNS equations are obtained by neglecting the streamwise viscous terms in the Navier-Stokes equations. When the viscous terms in the circumferential direction are also neglected, one gets the thin layer (TL) approximation.

The steady PNS or TL equations still have an elliptic nature (but of reduced order—see Sec. II) and therefore the initial value problem in the downstream marching direction is not well posed[2] A well-posed initial-boundary value problem can be formulated by specifying, for example, upstream and side conditions for the velocities and one downstream condition for the pressure. Therefore the PNS equations must be solved globally and cannot be solved by a single-sweep marching.

The reduced order of the PNS equations can be exploited by constructing an iterative marching method for updating the pressure field only[3] Such a multiple-sweep iteration method has the advantage that the velocity field is generated during the marching process and only the pressure field has to be stored from sweep to sweep—a considerable saving in storage results. However, simple-minded marching does not result in good convergence properties and sometimes diverges. For the two-dimensional case, Israeli and Lin[14] devised a stable marching scheme that behaves like the successive line over relaxation (SLOR) method for the solution of a single elliptic equation.

Rubin and Reddy[5] analyzed certain aspects of the solution of the PNS equations and used their procedure to solve several flow problems in Cartesian and axisymmetric body fitted conformal coordinates. They used in most cases a first-order scheme and also applied a simplified one-dimensional multigrid algorithm. Several more recent works are cited in Refs. 6-8.

The present study is a continuation of the work presented in Ref. 9, where the scheme of Israeli and Lin[14] was modified into a second-order, staggered, marching multigrid form. The principal aim here is to test the convergence properties of the methods in the case of viscous nonlinear problems and to apply the algorithm to several flow problems. The good smoothing properties of the Israeli and Lin scheme are used in a multigrid framework in order to accelerate the convergence of the solution of the PNS equations. The steady, incompressible, viscous, and two-dimensional equations are considered in a general curvilinear coordinate system. The marching scheme is implemented using a stable algorithm which is second-order accurate also in the marching direction. The same method can be used without modification for the incompressible Euler equations, as the effect of the Reynolds number on the convergence rate is insignificant. In two dimensions, the PNS and the TL equations are identical, and therefore the same analysis applies to both.

II. Formulation

The nondimensional steady, incompressible, and two-dimensional PNS (or TL) equations in a general curvilinear orthogonal coordinate system (ξ, η) are as follows:

Continuity

$$\frac{\partial(h_\xi V)}{\partial \eta} + \frac{\partial(h_\eta U)}{\partial \xi} = 0 \tag{1a}$$

Momentum, η

$$h_\xi \frac{V}{h_\eta} \frac{\partial V}{\partial \eta} + U \frac{\partial V}{\partial \xi} + \frac{UV}{h_\eta} \frac{\partial h_\eta}{\partial \xi} - \frac{U^2}{h_\eta} \frac{\partial h_\xi}{\partial \eta} = -\frac{J}{h_\eta^2} \frac{\partial P}{\partial \eta}$$

$$+ \frac{1}{Re} \frac{\partial}{\partial \eta} \left[\frac{1}{h_\eta^2} \frac{\partial}{\partial \eta}(h_\xi V) - h_\eta U \frac{\partial}{\partial \xi}\left(\frac{1}{h_\eta^2}\right) \right] \tag{1b}$$

Momentum, ξ

$$\frac{\partial U}{\partial \eta} + h_\eta h_\xi \frac{U}{\partial \xi} \frac{\partial U}{\partial \xi} + \frac{UV}{h_\xi} \frac{\partial h}{\partial \eta} - \frac{V^2}{h_\xi} \frac{\partial h_\eta}{\partial \xi} = -\frac{J}{h_\xi^2} \frac{\partial P}{\partial \xi}$$

$$+ \frac{1}{Re} \frac{\partial}{\partial \eta} \left[\frac{1}{J} \frac{\partial}{\partial \eta}(h_\xi U) + h_\eta V \frac{\partial}{\partial \xi}\left(\frac{1}{J}\right) \right] \tag{1c}$$

ξ is approximately aligned with the mainstream direction. U and V are the contravariant velocity components in the ξ and η directions respectively. P is the pressure and Re is the Reynolds number. h_ξ and h_η are the Lamme coefficients in the ξ and η directions. J is the Jacobian of the coordinate transformation.

The two-dimensional Navier-Stokes equations are elliptic of order four.[10] It can be shown that the PNS or TL equations are elliptic of order two only—like a single Poisson equation. This ellipticity is caused by the pressure gradient terms via the continuity equation. A well-posed problem can be formulated by defining the boundary conditions as described in Fig. 1 for a rectangular control volume. The following conditions may be specified:

Upstream boundary (AB)

$$U = U_{in} \qquad V = V_{in} \qquad (2a)$$

Solid wall (AD)

$$U = 0 \qquad V = 0 \qquad (2b)$$

Outer boundary (BC)

$$U = U_{out} \qquad P = P_{out} \qquad (2c)$$

Downstream boundary (CD)

$$\frac{\partial P}{\partial \xi} = \left(\frac{\partial P}{\partial \xi}\right)_{out} \qquad (2d)$$

Other boundary conditions can be used, but the same number of conditions on each boundary must be kept. Subscripts "in" and "out" refer to the inner and outer boundaries, respectively.

III. Discretization

Numerical solutions of Eqs. (1) are obtained by spreading a mesh over the computational domain. Let us assume that the grid points are distributed evenly along the ξ and η coordinates with the spacing Δ and $\Delta\eta$ respectively. When discretizing these equations it should be remembered that their nature should be reflected in the finite-difference approximation.[1,5] In order to be consistent with the boundary-layer (parabolic) nature of the flow, the axial gradients of the velocities should be computed using only upstream values, while the elliptic nature is preserved by forward differencing the axial pressure gradient.[1,5,8] Consequently, it was assumed that a stable marching scheme must be of the first order in the marching direction. But a second-order accuracy can be achieved by a judicious choice of the placement of the variables to be solved at each station. The choice can be explained most easily by considering a Cartesian coordinate system and taking $V = 0$ and $1/Re = 0$ in Eq. (1c), yielding

$$U_\xi^2 = -P_\xi \qquad (3)$$

A first-order difference scheme then becomes (see Fig. 2)

$$U_{m,j}^2 - U_{m-1,j}^2 = P_{m,j} - P_{m+1,j} \qquad (4)$$

with the unknowns $U_{m,j}$ and $P_{m,j}$. An alternative scheme, first suggested by Israeli[9,11] is written

$$U_{m,j}^2 - U_{m-1,j}^2 = P_{m-1,j} - P_{m,j} \qquad (5)$$

with the unknowns $U_{m,j}$ and $P_{m-1,j}$. The scheme is centered about $m + 1/2$ and is of second order.

The same applies to the full viscous PNS or TL equations. At each marching step one solves for all the velocities $U_{m,j}, V_{m,j}$, together with the pressure $P_{m-1,j}$, (for $j = 1, 2, \ldots, J$). Thus, the velocities are indeed solved using values from the upstream while the pressure uses information from the downstream. This approach was subsequently used in Refs. 3 and 8.

In addition, one may stagger the velocity V with respect to the other variables as shown in Fig. 2, where the centering points of the difference equations are also plotted. The differential equations are approximated by central second-order approximations. Whenever needed, averaging was used, as is usually done for staggered grids.

The nonlinear algebraic equations are linearized by either a full Newton-Raphson (NR) method or by performing only one NR iteration. The results are very similar, so usually a single NR iteration is used.

IV. The Multigrid Algorithm

The multigrid technique is a numerical procedure for substantially improving the convergence rate of iterative methods. In order to facilitate comparison with theory, the accommodative C-cycle MG algorithm was chosen.[10] Each MG process consists of three basic parts: relaxation, restriction, and interpolation.

Some of the elements of the present approach were used independently in Ref. 5. Detailed comparisons cannot be made because convergence rates were not presented there. In the present study the MG refinement is applied in both the ξ and η directions, whereas in Ref. 5 the computational mesh was refined only in the streamwise direction (one-dimensional MG procedure).

The Relaxation Scheme

The overall convergence rate of any MG process is strongly influenced by the smoothing properties of the relaxation scheme. It can be shown analytically and experimentally that the usual multiple-sweep marching does not have good con-
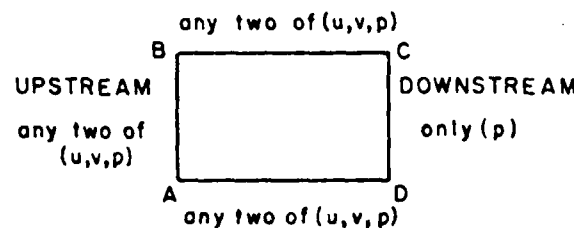

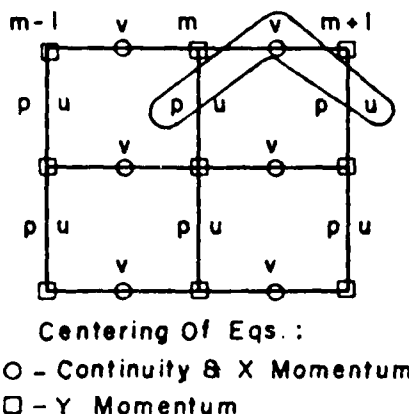Fig. 1 Example of permissible boundary conditions.

Centering Of Eqs. :

O – Continuity & X Momentum

□ – Y Momentum

Fig. 2 The staggered grid.

vergence and smoothing properties because short wave errors are not efficiently smoothed. Israeli and Lin[3,4] showed that certain modifications in the streamwise momentum equation which vanish upon convergence give rise to an iterative scheme that is equivalent in the linear case to the SLOR method for a single Poisson equation. In the general nonlinear case, the modified iterative process is essentially equivalent to the relaxation of a single nonlinear Poisson-like equation for the pressure. The velocities can be viewed as auxiliary variables needed during the marching since they have no "memory" by themselves.

Furthermore, the good smoothing properties of the line relaxation scheme of a single Poisson equation were automatically gained. The problems associated with the loss of ellipticity of the difference approximation for the Navier-Stokes equations at high Reynolds number[10] are thus avoided, and no upstream weighting or artificial viscosity is required. There results a considerable saving in storage as well as a simpler relaxation scheme where the convergence rate is essentially independent of the Reynolds number. The same marching algorithm can thus be used for the Euler equation with the same favorable convergence rate.

The extension of the marching scheme of Ref. 4 to a general curvilinear orthogonal coordinate system yields a modified mainstream momentum difference equation (the other difference equations remaining unchanged):

$$-G_m P^*_{m-1} = R_m + \tilde{S}_m \qquad (6a)$$

$$P^k_{m-1} = \omega P^*_{m-1} + (1-\omega) P^{k-1}_{m-1} \qquad (6b)$$

R_m includes the velocity terms of the finite-difference approximation. m is the marching step number, k is the global iteration index, and ω is the over-relaxation parameter. G_m and $\tilde{S}_m$ are given in Table 1. When the MG procedure is applied, the over-relaxation parameter is $\omega = 1$.

In each marching step, a block tridiagonal system is solved for the vectors U_m, V_m, and P_{m-1}; each component of the vectors corresponds to a point along the η coordinate. Thus, the continuity and the η-momentum difference equations are solved exactly in each step. The streamwise (ξ) momentum equation is not solved exactly since the pressure P_m, taken from the last global iteration, appears in it.

A linear von Neumann stability analysis of the marching iterative scheme for the primitive coupled system of difference equations of Eq. (1) in Cartesian coordinates (Z, Y) was performed by Rubin and Reddy.[5] They numerically determined the eigenvalues of the matrix of the relaxation process and found the estimate $\lambda_{max} = 1 - C_2(\Delta Z/Y_m)^2$ for $(\Delta Z/Y_m) \gg 1$. Y_m is the outer boundary in the normal Y direction; ΔZ is the interval in the marching direction Z. The rate of convergence is determined by the ratio $\Delta Z/Y_m$. They claim that this conclusion "...differs from that found for the

convergence analysis of line relaxation procedures for Poisson solvers. Although the source term S_{ij} leads to the conventional relaxation form of the Laplace operator for the pressure, the coupling with the velocities alters the structure of the inversion matrix and associated spectral radius."

It turns out, however, that the spectral radius λ_{max} can be determined analytically for the coupled PNS system and is independent, in the linear case, of the coupling by the velocities. A stability analysis of the discretized version of Eq. (1) using the modified form Eq. (6) reveals that the amplitude of the errors in the velocities can be related to the error in the pressure field. On the other hand, it was shown[3,4] that in the linearized case the global iteration scheme is reducible to the SLOR method for a single Poisson equation. It follows that all the known results from the theory of the SLOR scheme should be applicable to the present version of the global iterative scheme for the PNS equations. In particular, we find that the maximum eigenvalue λ_{max}, which determines the convergence rate, is given in the present case by[12]

$$(\lambda_{max} + \omega - 1)^2 = \lambda_{max} \omega^2 \mu^2_{max} \qquad (7a)$$

where

$$\mu_{max} = 1 / \left[1 - \left(\frac{\Delta Z}{\Delta Y} \right)^2 \left(1 - \cos\pi \frac{\Delta Y}{2Y_m} \right) \right] \qquad (7b)$$

for the boundary conditions of Eqs. (2) and with the appropriate scaling. Y_m and ΔY are the outer boundary and the interval in the Y direction respectively. For $\omega = 1$ the maximal eigenvalue is given by

$$\lambda_{max} \sim 1 - \tfrac{1}{4}(\pi\Delta Z/Y_m)^2 \qquad (7c)$$
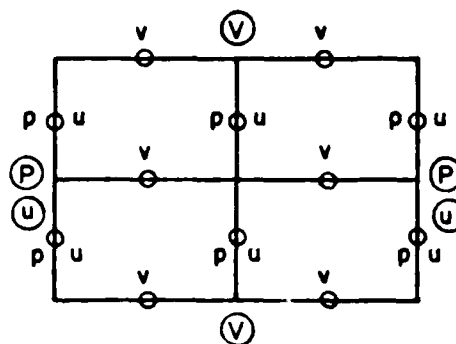
Fig. 3 Relative placement of the variables on two successive MG levels.

Table 1 Definition of G_m and $\tilde{S}_m$

m	G_m	$\tilde{S}_m$
2	$\left(\dfrac{J}{h^2_\xi}\right)_{m-1/2}$	$-\left(\dfrac{J}{h^2_\xi}\right)_{m-1/2} P_m$
3	$\left(\dfrac{J}{h^2_\xi}\right)_{m-1/2} + \left(\dfrac{J}{h^2}\right)_{m-1/2}$	$-\left(\dfrac{J}{h^2_\xi}\right)_{m-1/2} P_m - \left(\dfrac{J}{h^2_\xi}\right)_{m-3/2}(P_{m-1} - P_{m-2} + P^*_{m-1})$
4,5	$\left(\dfrac{J}{h^2_\xi}\right)_{m-1/2} + \left(\dfrac{J}{h^2}\right)_{m-1/2}$	$-\left(\dfrac{J}{h^2_\xi}\right)_{m-1/2} P_m - \left(\dfrac{J}{h^2_\xi}\right)_{m-3/2} P_{m-2}$ $+ \left[\left(\dfrac{J}{h^2_\xi}\right)_{m-3/2} + \left(\dfrac{J}{h^2_\xi}\right)_{m-5/2} \right] P^*_{m-2} + \tilde{S}_{m-1}$

Fig. 4 Convergence history on the finest grid for different relaxation schemes (linear scheme).

Fig. 5 Accuracy test of the pressure and the normalized skin friction coefficient at $Z = 4$ (semi-infinite flat plate).
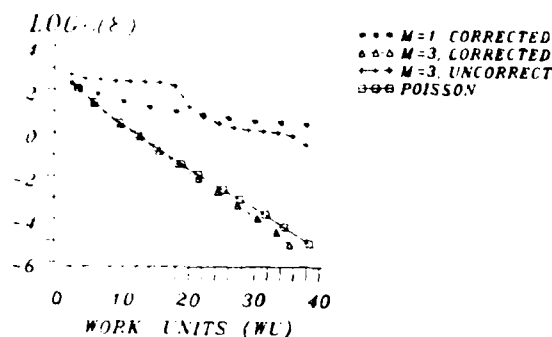
Numerical experiments verified the validity of Eq. (7c). For large enough $\Delta Z/Y_m$, the convergence is very rapid and no coarsening of the grid is necessary in the MG procedure. For smaller values of $\Delta Z/Y_m$, the MG procedure is invoked in order to accelerate convergence. For very small values of $\Delta Z/Y_m$, the MG scheme does not seem to be effective, and this indicates that the underlying relaxation scheme breaks down. Since the linear analysis assures convergence for all values of $\Delta Z/Y_m$, it is possible that nonlinear effects, which were neglected in the analysis, adversely affect the convergence rate and the smoothing properties of the relaxation.

Restriction and Storage Requirements

Let the finite-difference approximation of Eqs. (1) on the finest grid M be represented as in Ref. 10:

$$L_j^M \bar{W}^M(\bar{x}) = F_j^M(\bar{x}) \quad (8)$$

where $\bar{x} = [(\xi, \eta)]$, $\bar{W}^M = U^M, V^M, P^M]^T$ is the exact solution of the difference equations and j is the number of the differential equation ($j = 1,2,3$).

The problem is transferred in the full approximation storage (FAS) mode from the current level k to a coarser level $k - 1$ by correcting the right-hand side of Eq. (8) (see Fig. 3):

$$F^{k-1}(\bar{x}) = L_j^{k-1}\left[\bar{I}_k^{k-1}\bar{w}^k(\bar{x})\right] + I_{j,k}^{k-1}\left\{F_j^k(\bar{x}) - L_j^k\bar{w}^k(\bar{x})\right\} \quad (9)$$

$\bar{w}^k(\bar{x})$ is an approximation to $\bar{W}^k(\bar{x})$. $I_{j,k}^{k-1}$ and $\bar{I}_k^{k-1}$ are proper restriction operators for the jth equation and for the dependent variables, respectively.

The term within the braces in Eq. (9) is the residual of the jth equation. For the present marching scheme there is no residual in the continuity and in the η-momentum equations since they are solved exactly in each step. The residual of the ξ-momentum equation results only from the streamwise pressure gradient term, and its computation needs only one subtraction. $\bar{I}_k^{k-1}$ was chosen to be a linear interpolation, which yields $L_1^{k-1}[\bar{I}_k^{k-1}\bar{w}^k(\bar{x})] = 0$ for the continuity equation. $I_{j,k}^{k-1}$ is computed by averaging in both the ξ and η directions. $I_{2,k}^{k-1}$ is a simple injection. In summary, Eq. (9) takes the following form:

$$F_1^{k-1}(\bar{x}) = 0 \quad (10a)$$

$$F_2^{k-1}(\bar{x}) = L_2^{k-1}\left[\bar{I}_k^{k-1}\bar{w}^k(\bar{x})\right] \quad (10b)$$

$$F_3^{k-1}(\bar{x}) = L_3^{k-1}\left[\bar{I}_k^{k-1}\bar{w}^k(\bar{x})\right] + I_{3,k}^{k-1}\left[F_3^k - L_3^k\bar{w}^k(\bar{x})\right] \quad (10c)$$
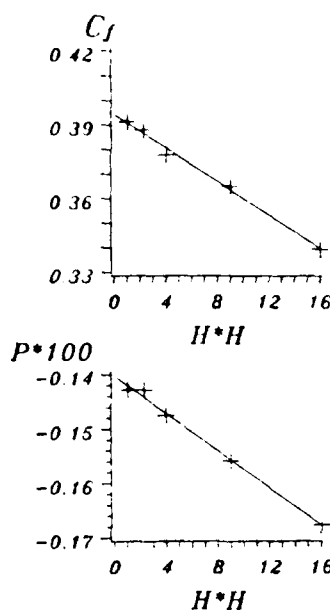
Two consequences should be emphasized: 1) only two corrections $[F_2^{k-1}(\bar{x}), F_3^{k-1}(\bar{x})]$ have to be computed and stored in the coarse grids, and 2) *all* the dependent variables must be transferred in order to compute the corrections $\{L_j^{k-1}[\bar{I}_k^{k-1}\bar{w}^k(\bar{x})]\}, j = 2,3\}$. Since only the pressure is stored, these corrections must be computed during the marching process.

Special attention must be paid to the restriction of the staggered flow variables at the boundaries in order to specify zero corrections as boundary conditions for the coarse grids. In the present study, all the boundary conditions were given at the physical boundaries. The values at the actual staggered placement of each variable at the boundaries were computed by averaging with inner points.

It follows that in addition to the pressure on all grids, one has to save one correction term for each momentum equation on the coarser grids. Assuming N computational points on the finest grid, a simple-minded estimate gives $14N/3$ storage locations for the two-dimensional NS multigrid solution and $2N$ for the PNS marching MG solution.

Interpolation

Since the present marching scheme generates the velocity field from the pressure field, only the correction to the pressure must be interpolated back to the fine grid:

$$P^{k+1} = P^{k+1} + I_k^{k+1}\left(P^k - \bar{I}_{k+1}^k P^{k+1}\right) \quad (11)$$

I_k^{k+1} is the interpolation operator. In the present case it is a linear operator.

The MG scheme described above is general. But so far only cases in Cartesian coordinate systems with equally spaced grid points were tested with the MG procedure.

V. Results

Linear Case

A linearized version of the PNS equations, expressed in a Cartesian coordinate system, has been tested in Ref. 9. Some of the results are presented here for reference and for comparison with the nonlinear solutions.

Figure 4 compares the convergence history of different relaxation schemes with and without MG acceleration for a
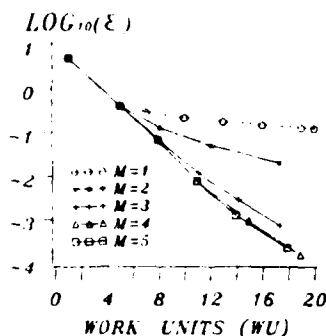
Fig. 6   Convergence history on the finest grid (semi-infinite flat plate).

Fig. 7   The pressure profile at $Z = 3$ (semi-infinite flat plate).

finest grid consisting of 17×17 mesh points. The horizontal axis gives the number of work units (WU).[10] A work unit is equivalent to one global iteration on the finest grid. The vertical axis gives the dynamic residual. The MG procedure with three levels ($M = 3$) shows a much better convergence rate than the single grid solution for the same problem. The convergence factor per relaxation iteration (see Ref. 10 for definition) for $M = 3$ is $\bar\mu = 0.60$, whereas for the single grid case ($M = 1$) $\bar\mu = 0.97$. The linearized PNS equations were also solved without the streamwise correction of Refs. 3 and 4. The MG convergence factor is much worse ($\bar\mu = 0.79$). Upon increasing the number of grid points, the unmodified equation's convergence deteriorates. As one can expect, the corrected equations and the solution of the equivalent single Poisson equation for the pressure exhibit very similar convergence properties.

Nonlinear Cases

A series of flow problems were solved with the nonlinear PNS equations. Several test cases were run in a Cartesian coordinate system with possible clustering of mesh points by one-dimensional stretching functions in each direction. Among them we shall mention the flow over an infinite, a semi-infinite, and a finite flat plate, trailing edge flow and an entrance flow between two flat plates. Two cases were run with curvilinear orthogonal coordinate systems: the flow along an axisymmetric cylinder and the flow over a prolate spheroid at zero angle of attack. In the following sections some of the cases will be detailed.

Semi-Infinite Flat Plate

In this case the flow is computed starting from the leading edge, where a uniform velocity $U = 1$, $V = 0$ is given. The downstream boundary was set at $Z = \xi = 4$ and zero pressure gradient was specified there as $\partial P/\partial Z = 0$. On the outer boundary, $U = 1$ and $P = 0$. The no-slip and no-injection conditions were used at the plate.

The second-order accuracy convergence of the finite-difference equations is demonstrated in Fig. 5. The pressure at a fixed point and the normalized skin friction $C_f = C_F\sqrt{Re \cdot Z}$ (which is proportional to the main velocity gradient) at $Z = 4$ are plotted against H^2; H is proportional to the mesh interval.

The convergence history on a finest grid consisting of 65×65 points is shown in Fig. 6 for $Re = 10^3$. The outer boundary is placed at $Y_{max} = 1$ where Y is the normal coordinate ($Y = \eta$). Increasing the number of levels M increases the convergence rate until $M = 4$. The convergence factor per relaxation ($\bar\mu = 0.562$) is close to the theoretical value obtained for the solution of a single Poisson equation with the SLOR method ($\bar\mu = 0.547$).

For $Re = 10^4$ and $Z = 3$, the pressure distribution as a function of the Blasius similarity coordinate $\zeta = y\sqrt{Re/Z}$ is
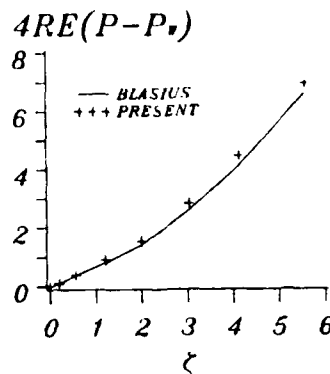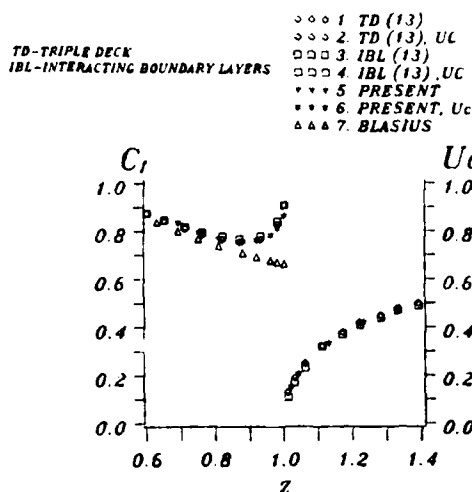

Fig. 8   Normalized skin friction coefficient and wake centerline velocity development (trailing edge flow).

shown in Fig. 7. The distance from the leading edge is large enough to satisfy the Blasius assumptions; the skin friction coefficient deviates no more than 3% from the theoretical value. The computed pressure is compared with the "Blasius pressure" that can be obtained from the normal momentum equation

$$4ReZ(P - P_w) = f(\zeta f' - f) + 2\zeta f'' \qquad (12)$$

P_w is the pressure on the plate. f is the solution of the Blasius boundary-layer equation for a flat plate with zero pressure gradient. f' and f'' are the first and second derivatives with respect to ζ. The agreement between the present computations and Eq. (12) is good.

Trailing Edge Flow

The Reynolds number was fixed at $Re = 10^5$ and a grid of 65×73 points was used. The flat plate with zero thickness occupies the interval $[0,1]$ along the $Z(=\zeta)$ axis. We assumed that the interaction is limited to the interval $0.5 < Z < 1.5$. The Blasius solution was specified at the upstream boundary ($Z = 0.5$) and symmetry boundary conditions were given behind the plate. The Blasius solution was approximated by the fourth-order Karman-Pohlhausen velocity profile.

Figure 8 shows the normalized skin friction coefficient ($C_f = C_F\sqrt{Re}$) on the plate ($Z < 1$) and the wake centerline velocity (U_c, $Z > 1$). The agreement with the interacting

boundary layers (IBL) solution and with the triple deck (TD)[13] result is satisfactory.

Entrance Flow Between Two Flat Plates

Uniform inlet conditions were specified at the entrance $(U = 1, V = 0)$ while the usual no-slip and no-injection conditions were given at the plates. At the downstream boundary the pressure gradient was calculated by assuming a fully developed flow

$$\frac{\partial P}{\partial Z} = -\frac{12\dot{m}}{Re} \tag{13}$$

$\dot{m}$ is the rate of mass flow.

Figure 9 shows the development of the centerline velocity for two Reynolds numbers, $Re = 20$ and 200, and for a grid of 41×101 points. The results are compared with the full Navier-Stokes computations of Ref. 14. Again the agreement is satisfactory, even at the entrance where the omission of the streamwise diffusion terms may be questionable.

Prolate Spheroid at Zero Angle of Attack

This test case is more stringent because a curvilinear orthogonal prolate spheroid coordinate system is used and the flowfield is more complex than in the previous cases.[15] A nonzero pressure gradient exists at the outer boundary: favorable at the front half and adverse in the rear half. The flowfield eventually separates, with reversed flow near the spheroid. Several numerical solutions of the present problem exist,[15-17] but all of them use the boundary-layer approximation.

The flowfield was computed for a region between the nose and the rear part of the spheroid. The analytically known potential flow is specified at the outer boundary (U and P) and at the downstream boundary $(\partial P/\partial\xi)$. At the spheroid the no-slip and no-injection conditions is given. At the up-

stream boundary the two velocity components are specified. Usually they can be computed from a boundary-layer code. In the present work, the approximate main velocity was computed from a Karman-Pohlhausen profile with a specified skin friction coefficient or displacement thickness. The specified quantity was taken from existing boundary-layer solutions of the same case. The normal component of the velocity V was determined from the potential solution. Numerical experiments show that for reasonable upstream conditions the solution is independent of the upstream conditions, apart from the first few marching steps.

The downstream boundary was set before the separated zone, although the PNS equations are valid there. The computation of flowfields with reversed main flow needs modifications in the approximation of the convection terms.

Two thickness ratios of the axes were considered—4:1 and 6:1. In each case the Reynolds number was $Re = 10^6$ and a single grid consisting of 17×65 points was used (in the η and ξ directions respectively).

Thickness Ratio 4:1

The dependence of the normalized skin friction coefficient $(C_f = C_f\sqrt{Re})$ on the axial distance $(Z = \cos\xi)$ is shown in Fig. 10. It compares well with the boundary-layer solution of Ref. 16 but disagrees with Wang's solution.[15]

The point of separation is determined where C_f vanishes. In the present case, the separation point was found to be at

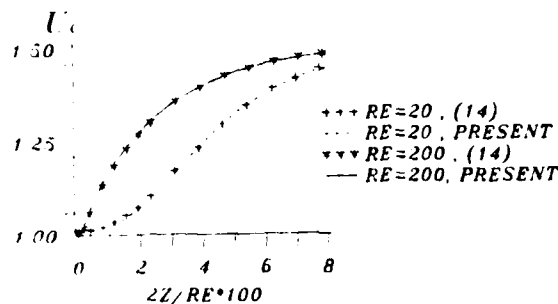Fig. 11　The pressure distribution along the spheroid of thickness 6:1.

Fig. 9　The development of the centerline velocity (entrance flow).
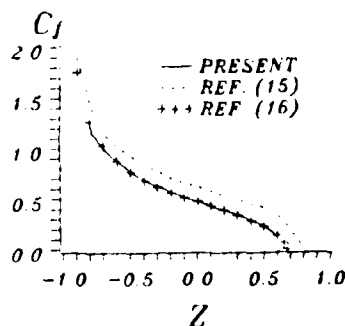
Fig. 10　The distribution of the skin friction coefficient along the spheroid of thickness 4:1.
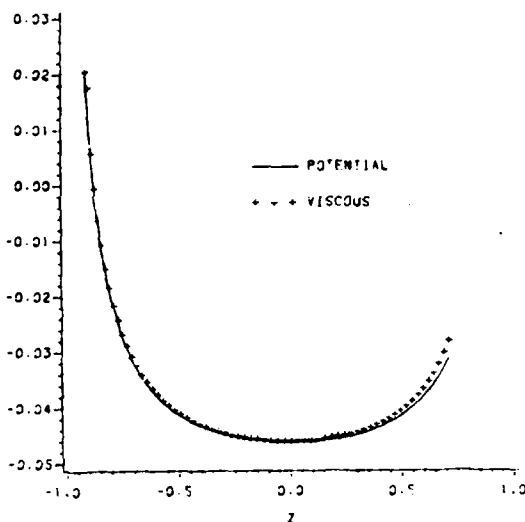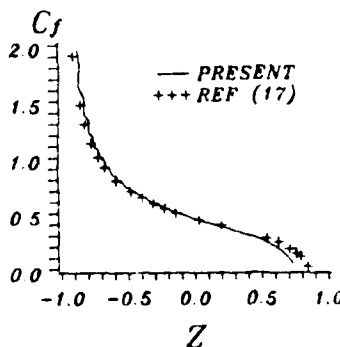
Fig. 12　The distribution of the skin friction coefficient along the spheroid of thickness 6:1.
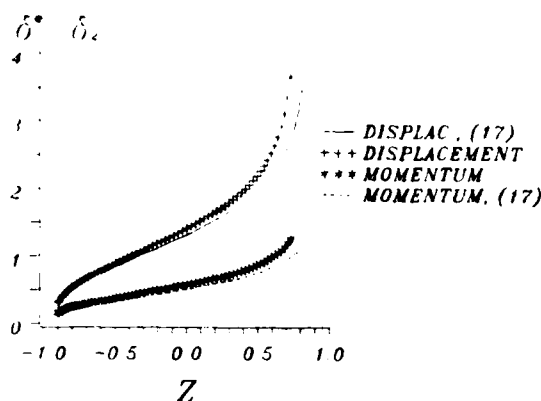
Fig. 13 The development of the integral thicknesses along the spheroid of thickness 6:1.

$Z = 0.67$, which is in excellent agreement with Refs. 16 and 17. Wang[15] has computed the separation point at $Z = 0.84$.

Thickness Ratio 6:1

The pressure distribution on the spheroid, as is found in the PNS solution, is compared with the potential solution in Fig. 11. The agreement is very good except near the downstream boundary. It demonstrates the validity of the boundary-layer approximation for the computation of unseparated flow regions over slender bodies. The slight disagreement near the downstream may be attributed to the improper value being given for the downstream pressure gradient. The potential pressure gradient, as was chosen in this case, is not a good choice near regions of separation.

The skin friction coefficient distribution is compared with a boundary-layer calculation of Schoenauer[17] in Fig. 12. The agreement is good except near the upstream and downstream boundaries. The disagreement in the upstream region probably results from unsatisfactory initial conditions for the velocities. The separation point is found to be closer to the nose ($Z = 0.77$) than in Ref. 17 ($Z = 0.87$), presumably because of the greater adverse pressure gradient computed from the PNS solution. For this more slender body, the separation point is further downstream than in the previous case (with the thickness ratio 4:1).

Figure 13 gives the displacement (δ^*) and the momentum (δ_z) thicknesses dependence on Z. The values computed in the present work are higher than in Ref. 17. The difference is more pronounced near the separation point.

VI. Conclusion

In the present study, an iterative marching method for the solution of the PNS equations is extended to curvilinear orthogonal coordinate systems. Stable second-order-accurate finite-difference equations were developed using central approximation to all derivatives. The solution algorithm is basically equivalent to the solution of a single elliptic equation with the SLOR method. The efficient two-dimensional MG procedure previously developed for a linearized PNS equation was applied to the solution of several nonlinear viscous flows

in Cartesian grids. The convergence rates were not adversely affected by the nonlinearity.

References

[1]Rubin, S.G., "Global Relaxation Procedure for a Reduced Form of the Navier-Stokes Equations," *Proceedings of the Ninth International Conference on Numerical Methods in Fluid Dynamics, Lecture Notes in Physics*, Vol. 218, Springer-Verlag, 1985, pp. 62–71.

[2]Israeli, M., Reitman, V., Salomon, S., and Wolfshtein, M., "On the Marching Solution of the Elliptic Equations in Viscous Fluid Mechanics," *Proceedings of the Second International Conference on Numerical Methods in Laminar and Turbulent Flows*, edited by C. Taylor and B.A. Schrefler, Venice, 1981, pp. 3–14.

[3]Israeli, M. and Lin, A., "Numerical Solution and Boundary Conditions for Boundary Layer Like Flows," *Proceedings of the Eighth International Conference on Numerical Methods in Fluid Dynamics, Lecture Notes in Physics*, Vol. 170, Springer-Verlag, 1982, pp. 266–272.

[4]Israeli, M. and Lin, A., "Iterative Numerical Solutions and Boundary Conditions for the Parabolized Navier-Stokes Equations," *Computers and Fluids*, Vol. 13, No. 4, 1985, pp. 397–409.

[5]Rubin, S.G. and Reddy, D.R., "Analysis of Global Pressure Relaxation for Flows with Strong Interaction and Separation," *Computers and Fluids*, Vol. 11, No. 4, 1983, pp. 281–306.

[6]Khosla, P.K. and Lai, M.T., "Global PNS Solutions for Subsonic Strong Interaction Flow Over a Cone-Cylinder-Boattail Configuration," *Computers and Fluids*, Vol. 11, No. 4, 1983, pp. 325–339.

[7]Khosla, P.K. and Bender, E.E., "Solution of Parabolized Navier-Stokes Equations for Three-Dimensional Internal Flows," *Proceedings of the Ninth International Conference on Numerical Methods in Fluid Dynamics, Lecture Notes in Physics*, Vol. 218, Springer-Verlag, 1985, pp. 296–301.

[8]Reddy, D.R. and Rubin, S.G., "Subsonic/Transonic Viscous/Inviscid Relaxation Procedures for Strong Pressure Interactions," AIAA Paper 84-1627, June 1984.

[9]Israeli, M. and Rosenfeld, M., "Marching Multigrid Solutions to the Parabolized Navier-Stokes (and Thin Layer) Equations," *Proceedings of the Fifth GAMM Conference on Numerical Methods in Fluid Mechanics, Notes on Numerical Fluid Mechanics*, Vol. 7, 1984, pp. 137–144.

[10]Brandt, A. and Dinar, N., "Multigrid Solution to Elliptic Flow Problems," *Numerical Methods for PDE's*, Academic Press, Inc., New York, 1979, pp. 53–147.

[11]Israeli, M., "*Marching Solutions of PNS Equations*," NASA Lewis Seminar, NASA Lewis Research Center, Cleveland, OH, July 1982.

[12]Forsythe, G.E. and Wasow, W.R., "Finite-difference Methods for Partial Differential Equations," Wiley, New York, 1960, pp. 266–271.

[13]Veldman, A.E.P., "New, Quasi-Simultaneous Method to Calculate Interacting Boundary Layers," *AIAA Journal*, Vol. 19, Jan. 1981, pp. 79–85.

[14]Morihara, H. and Cheng, R.T.S., "Numerical Solution of the Viscous Flow in the Entrance Region of Parallel Plates," *Journal of Computational Physics*, Vol. 11, No. 4, 1973, pp. 550–572.

[15]Wang, K.C., "Three-dimensional Boundary Layer Near the Plane of Symmetry of a Spheroid at Incidence," *Journal of Fluid Mechanics*, Vol. 43, Pt. 1, 1970, pp. 187–209.

[16]Hirsh, R.S. and Cebeci, T., "Calculation of Three-Dimensional Boundary Layers with Negative Cross Flow on Bodies of Revolution," AIAA Paper 77-683, June 1977

[17]Schoenauer, W., private communication, 1985.

END
DATE
FILMED

5-88

DTIC